Article

Single Residue Variation in Skeletal Muscle Myosin Enables Direct and Selective Drug Targeting for Spasticity and Muscle Stiffness

Graphical Abstract

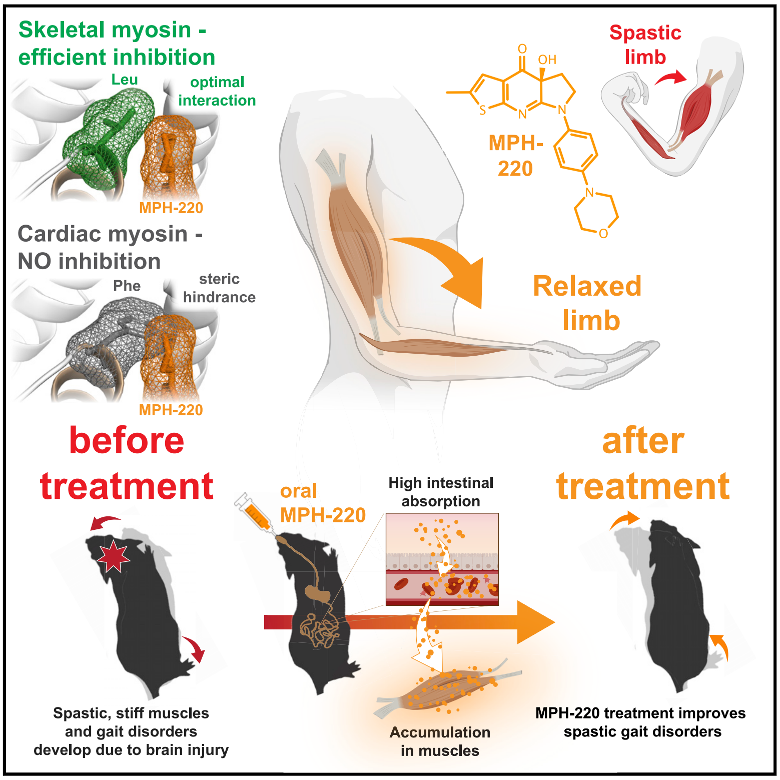

Highlights

- A key residue variation of fast skeletal myosin allows selective targeting
- A rationally designed inhibitor (MPH-220) specifically blocks skeletal muscle
- The inhibitor-bound myosin atomic structure reveals mechanism of selectivity
- MPH-220 improves gait disorders in spastic animal model after brain injury

Authors

Máté Gyimesi, Ádám I. Horváth,
Demeter Túrós, ..., Sámuel Komoly,
Anne Houdusse,
András Málnási-Csizmadia

Correspondence

mate.gyimesi@elte.hu (M.G.),
malna@elte.hu (A.M.-C.)

In Brief

Therapeutic muscle relaxation is currently achieved pharmacologically via indirect mechanisms by modulation of the nervous system. Selective targeting of skeletal muscle has not been possible because myosin isoforms in skeletal muscle and the heart are structurally very similar. Using a rational, structure-based approach, Gyimesi et al. design a small-molecule muscle relaxant that specifically inhibits the skeletal, but not the cardiac, myosin 2 isoform. With their new drug candidate, they show how spasticity and muscle stiffness might be relieved pharmacologically without cardiac or nervous system side effects.

Gyimesi et al., 2020, Cell *183*, 335–346
October 15, 2020 © 2020 Elsevier Inc.
https://doi.org/10.1016/j.cell.2020.08.050

Cell

CellPress

Article

Single Residue Variation in Skeletal Muscle Myosin Enables Direct and Selective Drug Targeting for Spasticity and Muscle Stiffness

Máté Gyimesi,[1,2,*] Ádám I. Horváth,[1] Demeter Túrós,[1] Sharad Kumar Suthar,[1,3] Máté Pénzes,[1] Csilla Kurdi,[1] Louise Canon,[4] Carlos Kikuti,[4] Kathleen M. Ruppel,[5] Darshan V. Trivedi,[5] James A. Spudich,[5] István Lőrincz,[3] Anna Á. Rauscher,[1,2] Mihály Kovács,[1,6] Endre Pál,[7] Sámuel Komoly,[7] Anne Houdusse,[4] and András Málnási-Csizmadia[1,6,8,*]
[1]MTA-ELTE Motor Pharmacology Research Group, Pázmány Péter sétány 1/c, 1117 Budapest, Hungary
[2]Motorpharma, Ltd., Szilágyi Erzsébet fasor 27, 1026 Budapest, Hungary
[3]Printnet, Ltd., Kisgömb utca 25-27, 1135 Budapest, Hungary
[4]Structural Motility, Institut Curie, Paris Université Sciences et Lettres, Sorbonne Université, CNRS UMR144, 75005 Paris, France
[5]Department of Biochemistry, Stanford University School of Medicine, Beckman Center B400, 279 W. Campus Drive, Stanford, CA 94305, USA
[6]Department of Biochemistry, Eötvös Loránd University, Pázmány Péter sétány 1/c, 1117 Budapest, Hungary and Brunszvik u. 2, 2462 Martonvásár, Hungary
[7]Department of Neurology, University of Pécs, Rét utca 2, 7623 Pécs, Hungary
[8]Lead Contact
*Correspondence: mate.gyimesi@elte.hu (M.G.), malna@elte.hu (A.M.-C.)

https://doi.org/10.1016/j.cell.2020.08.050

SUMMARY

Muscle spasticity after nervous system injuries and painful low back spasm affect more than 10% of global population. Current medications are of limited efficacy and cause neurological and cardiovascular side effects because they target upstream regulators of muscle contraction. Direct myosin inhibition could provide optimal muscle relaxation; however, targeting skeletal myosin is particularly challenging because of its similarity to the cardiac isoform. We identified a key residue difference between these myosin isoforms, located in the communication center of the functional regions, which allowed us to design a selective inhibitor, MPH-220. Mutagenic analysis and the atomic structure of MPH-220-bound skeletal muscle myosin confirmed the mechanism of specificity. Targeting skeletal muscle myosin by MPH-220 enabled muscle relaxation, in human and model systems, without cardiovascular side effects and improved spastic gait disorders after brain injury in a disease model. MPH-220 provides a potential nervous-system-independent option to treat spasticity and muscle stiffness.

INTRODUCTION

Spasticity—characterized by involuntary increased tone of skeletal muscles—is a common sensorimotor disorder in patients with brain and spinal cord injuries after stroke, trauma, cerebral palsy, or in multiple sclerosis and several myopathies of different etiologies (Li, 2017; Trompetto et al., 2014). Spasticity-related physical and mental conditions of patients often permanently disable self-supporting life management and ability to work (Martin et al., 2014; Rychlik et al., 2016). Economic burden for post-stroke patients with spasticity is 4-fold higher than those for patients without spasticity (Zorowitz et al., 2013), which includes direct costs of medications and hospitalization and indirect costs of caregiver assignments and independent daily-life-facilitating instruments.

Spasticity develops as a consequence of complex rearrangements of supraspinal inputs, which transforms the synaptic regulation of motoneurons that drives muscle contraction. The resulting exaggerated stretch reflex is accompanied with disrupted balance in regulation from the premotor cortex and reticular formation of the brainstem, which finally leads to aberrantly increased potentiation of motoneurons and hypercontraction of muscles (Enslin et al., 2020; Mukherjee and Chakravarty, 2010; Trompetto et al., 2014).

Current muscle relaxants in medical practice target the central nervous system (e.g., baclofen [GABA$_B$ agonist] and tizanidine [α2 agonist]), the neuromuscular junction (botulinum toxins), or the sarcoplasmic reticulum in muscle cells (dantrolene; Figure 1A). Due to their aspecific mechanism of action, centrally acting muscle relaxants have a wide range of neurological and cardiovascular side effects (drowsiness, dizziness, depression, and low blood pressure; Meleger, 2006; Smit and Slim, 2008) and low levels of efficacy (Orsnes et al., 2000), which often necessitate the application of an intrathecal pump surgically

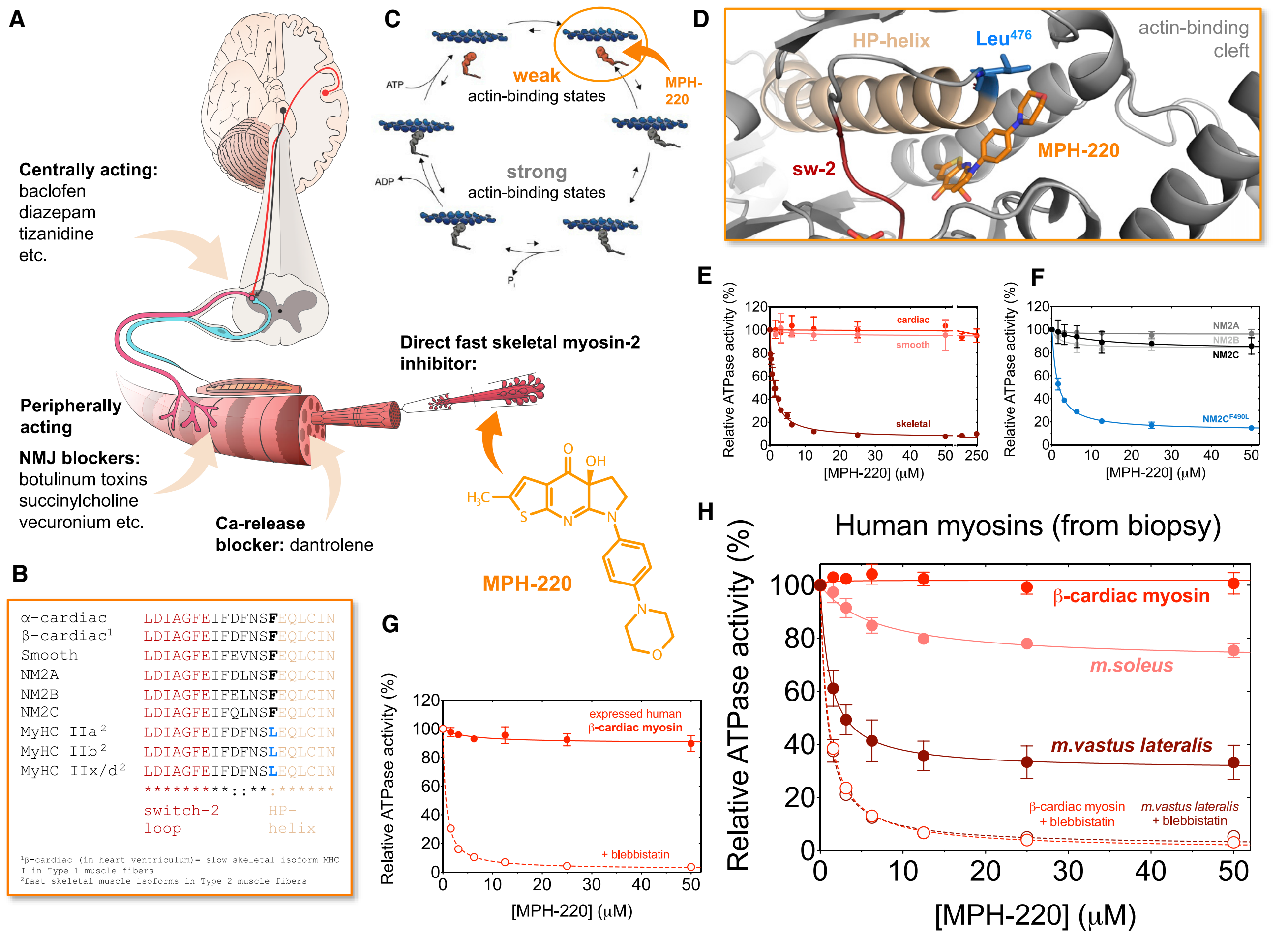

Figure 1. MPH-220 Inhibits Skeletal Muscle Myosin with Extreme Selectivity Independently of the Nervous System

(A) Current muscle relaxants target the central nervous system or act peripherally, whereas MPH-220 directly inhibits myosin.

(B) Human myosin-2 isoforms contain phenylalanine (black F) at the beginning of the HP-helix between the switch-2 loop (red) and the relay region, except for fast skeletal myosin isoforms, where this position is leucine (blue L; cf. Figure S1).

(C) MPH-220 was designed to bind into the blebbistatin-binding cavity of the motor domain, to enable inhibition in the actin-detached state.

(D) Close-up view of the communication center of the functional regions (actin-binding cleft, switch-2 loop of the active site, and the HP-relay-converter region) in the homology model of MyHC IIa with bound MPH-220 (orange) reveals interaction between the morpholino group and Leu^{476} in the HP-helix.

(E) Actin-activated ATPase inhibition of three myosin-2 isoforms (cf. Table S1).

(F) Actin-activated ATPase inhibition of NM2A, NM2B, NM2C and the NM2C^{F490L} variant.

(G) Actin-activated ATPase inhibition of expressed human β-cardiac myosin with MPH-220 and blebbistatin.

(H) Actin-activated ATPase inhibition of human muscle myosin samples from biopsies of *m. soleus*, *m. vastus lateralis*, and heart ventricle. In contrast to MPH-220, blebbistatin fully inhibited *m. vastus lateralis* sample and β-cardiac myosin samples. Mean ± SD are shown in all ATPase experiments; n = 3–9.

See also Figures S1 and S2.

implanted inside the body (Medical Advisory, 2005). Systemic treatment with botulinum toxins is impossible due to their lethal effect on respiratory and cardiac functions, and local treatments are painful, costly, and often ineffective (Careta et al., 2015; Pavone et al., 2016). Dantrolene has been associated with severe hepatotoxicity and genotoxicity (NIH, 2012); therefore, its clinical use is now restricted to life-threatening malignant hyperthermia. Surgical treatment of severe spasticity is limited to selective dorsal rhizotomy, when the sensory roots that transfer abnormal information from the muscles to the spinal cord are transected. However, the advantage of dorsal rhizotomy over oral medications is only marginal, because the treatment often leads to paralysis, chronic back pain, sensory dysfunction, inflammation, constipation, and cyst formation in the spinal column (cf. NICE interventional guidance 373).

Besides nervous-system-injury-related spasticity, permanent muscle spasms emerge as the leading source of prolonged pain in non-specific low back pain and chronic musculoskeletal pain disorder, fibromyalgia, altogether affecting more than 10% of global population (Marques et al., 2017; Vos et al., 2012). Although treatments of muscle spasm in these syndromes with systemic muscle relaxants are statistically effective, recommendations for their use in clinics underline precautions due to the reported adverse side effects resulting from non-specific targeting of the nervous system (Tofferi et al., 2004; van Tulder et al., 2003).

These considerations emphasize the unmet medical need for the development of a new-generation anti-spastic drug, which directly targets the effector protein of muscle contraction while avoiding neurological and cardiovascular side effects. Nervous-system-independent inhibition of muscle contraction in spastic patients could also overcome the need for targeting the otherwise disrupted synaptic balance of neuronal regulation.

Selective inhibition of skeletal muscles, however, raises the challenge of developing a small molecule that distinguishes between the structurally and sequentially highly similar myosin-2 isoforms. The ideal candidate inhibits only skeletal muscle fast isoforms (MyHC IIa,b,x/d), because the slow isoform in skeletal muscles (myosin heavy chain [MyHC I]) expressed from the *MYH7* gene is identical to β-cardiac myosin, the most abundant motor in the ventricles of the heart (Coluccio, 2020; Figures 1B and S1).

RESULTS

In order to relax muscle fibers, we aimed to arrest the actomyosin force-generation cycle in the actin-detached weak actin-binding state (Takács et al., 2010), when myosin heads are decoupled from actin filaments (Málnási-Csizmadia and Kovács, 2010; Sweeney and Hammers, 2018; Figure 1C). Using rational pharmacological design in a model MyHC IIa myosin structure, we developed and optimized a small-molecule inhibitor (MPH-220) into the myosin-2 class-specific blebbistatin-binding pocket (Allingham et al., 2005; Kovács et al., 2004; Limouze et al., 2004; Straight et al., 2003; Figures 1D and S2). MPH-220 enabled selective inhibition of fast skeletal myosin-2 isoforms (further referred to as skeletal myosins; Figure S1) isolated from rabbit psoas muscle, whereas—even at extremely high concentrations—it did not inhibit the ATPase activity of slow skeletal/β-cardiac myosin (further referred to as cardiac myosin) isolated from left ventricle of porcine heart or smooth muscle myosin-2 (Figure 1E; Table S1) or any non-muscle myosin-2 (NM2) isoforms (Figure 1F; Table S1). Sequence analysis of the inhibitor binding site revealed an important difference between the cardiac and skeletal myosins near the morpholine ring of MPH-220 at a location playing a key role in the myosin force-generation pathway (Málnási-Csizmadia and Kovács, 2010). The drug-interacting amino acid is uniquely and invariably leucine in fast skeletal myosin heavy chains (Leu^{476} in human MyHC IIa), whereas this position is occupied by phenylalanine in all other myosin-2 isoforms (Figures 1B and S1). We hypothesized that this structural difference can be the basis for the extreme selectivity of MPH-220 toward skeletal myosins. Therefore, we assessed the role of a Phe/Leu exchange through mutational analysis of human non-muscle myosin-2C (NM2C), which is not inhibited by MPH-220 in the wild-type form, possibly due to the presence of Phe^{490} in the corresponding position. According to our hypothesis, the expressed NM2C^{F490L} variant became sensitive to MPH-220 (Figure 1F), corroborating that the single-amino-acid change determines the observed selectivity.

Considering the selective inhibitory nature of MPH-220 on myosin samples (Figures 1E and 1F) and its potential to become a new-generation anti-spastic drug candidate, we performed ATPase inhibition assays on human myosin samples. Expressed human β-cardiac myosin was essentially unaffected by MPH-220, however, the non-selective myosin-2 inhibitor, blebbistatin, completely blocked its ATPase activity (Figure 1G; Table S1). We further tested MPH-220 on skeletal and cardiac myosin samples isolated from patient-derived biopsies (Figure 1H; Table S1). In line with their myosin-2 isoform composition, skeletal myosin samples from *m.vastus lateralis* and *m.soleus*—containing 56% and 28% fast isoforms in human muscles (Figure S1)—were inhibited by 70% and 29%, respectively, confirming the hypothesis that only the fast isoform fraction is targeted by MPH-220. More importantly, β-cardiac myosin isolated from human heart left ventricle was unaffected by MPH-220 (Figure 1H; Table S1). By contrast, blebbistatin reduced the activity of *m.vastus lateralis* and cardiac myosin samples by more than 90%, confirming that MPH-220 inhibition is proportional to the ratio of fast myosin isoform in different tissues (Figure 1H; Table S1). These results provide the basis for future safe systemic administration of MPH-220 to human patients. Left ventricle human biopsy contains cca. 10% α-cardiac myosin isoform (expressed from the *MYH6* gene [Figure S1; Miyata et al., 2000], which also contains Phe in the proximal part of HP-helix Phe^{474}). The lack of inhibition of myosin samples from the biopsies confirms that α-cardiac myosin could not be inhibited by MPH-220. We also note that gene products of MYH1, MYH2, and MYH4 encoding fast skeletal muscle myosin heavy chains IIx/d, IIa, and IIb, respectively, are not expressed in adult human heart in significant amount (England and Loughna, 2013; NCBI Gene Expression database).

In order to further analyze the molecular background of selectivity, we crystalized fast skeletal muscle myosin (isolated from high-quality rabbit *m.psoas*) in the presence of MPH-220 (Figures 2A and S3). The crystal structure confirmed that MPH-220 binds to the blebbistatin-binding cleft and its morpholine ring is in close proximity to Leu^{476}. This residue is at the N terminus of the so-called HP-helix of the L50 subdomain (Cope et al., 1996), which is preceded by the switch-2 loop and followed by the relay region of the motor. Comparison of the MPH-220-bound skeletal and blebbistatin-bound *Dictyostelium* myosin-2 structures confirms that, although the tricyclic cores of the inhibitors, including the chiral OH, are positioned similarly, Phe^{466} of the HP-helix in *Dictyostelium* myosin-2 comes into steric hindrance with MPH-220 (Figure 2B). Likewise, the position of this Phe in cardiac myosin structure also causes steric hindrance with MPH-220 (Planelles-Herrero et al., 2017; Figure 2C). This steric hindrance based on crystal structures together with the biochemical results strongly support that the unique Leu in the HP-helix of fast skeletal muscle myosin isoforms is responsible for the extreme selectivity of MPH-220. This mechanism for selective inhibition among myosin-2 isoforms is analogous to how blebbistatin is selective for myosin-2s due to the presence of the switch-2 Ser/Ala residue in myosin-2s (Allingham et al., 2005), whereas this position is occupied by Tyr/Phe in myosins from other classes that are uninhibited by blebbistatin. The resolved crystal structure also confirmed that MPH-220 selects and stabilizes the pre-powerstroke state. Overall, the structure

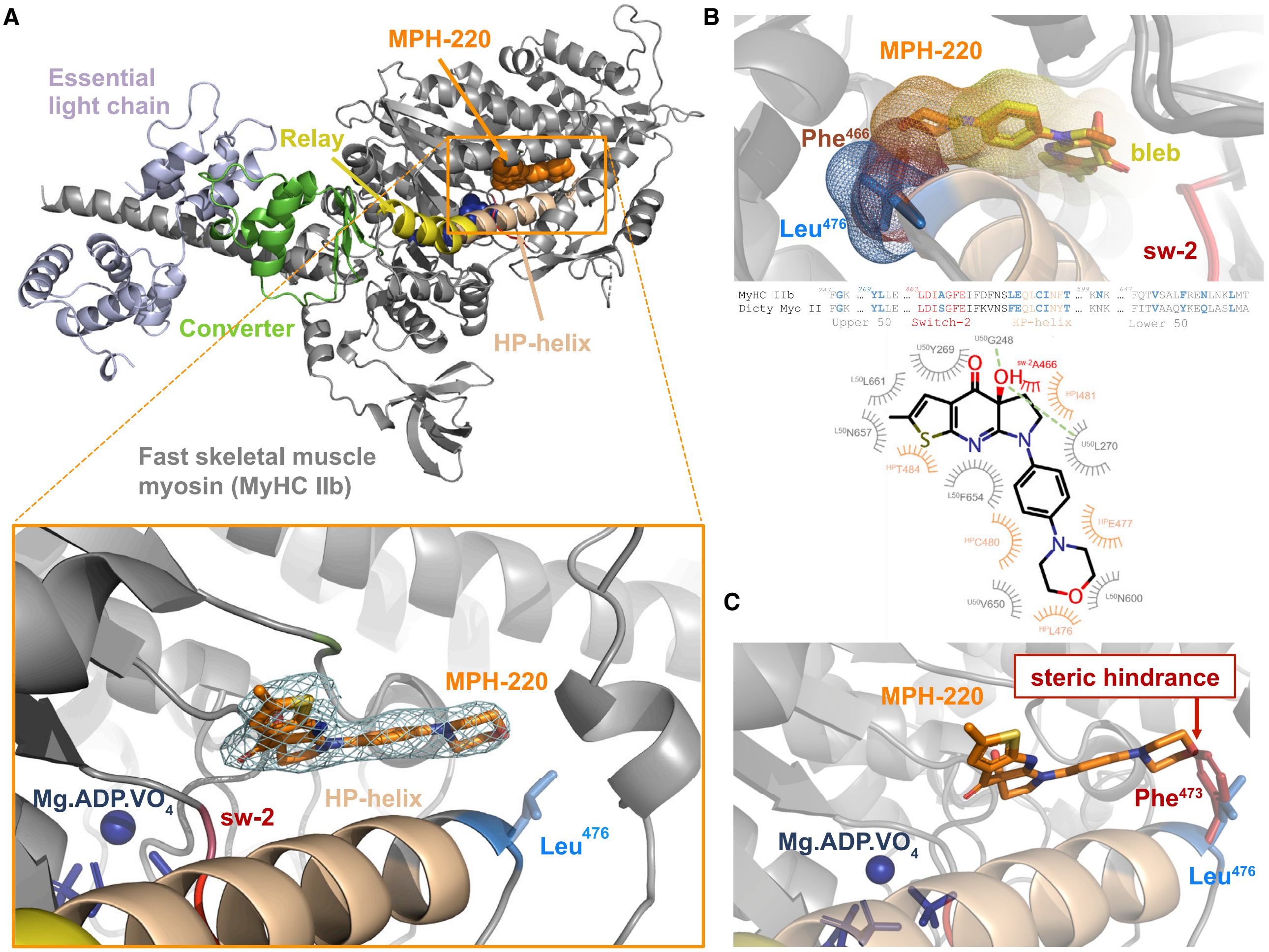

Figure 2. Crystal Structure of MPH-220-Bound Fast Skeletal Muscle Myosin

(A) Cartoon representation of the heavy chain (gray) of rabbit skeletal muscle myosin-2 in Mg.ADP.VO_4 (spheres, blue) pre-powerstroke state with the essential light chain bound to the lever arm. MPH-220 binds to the bottom of the actin-binding cleft close to the HP-helix, with its morpholine ring in close proximity of Leu^{476}. Blue mesh, electron density corresponding to MPH-220 at sigma 1.0.

(B) Comparison of the MPH-220 (orange) binding site in MyHC IIb (gray/beige) and the blebbistatin (yellow) binding site in *Dictyostelium* myosin-2 (dark gray/brown; PDB: 1YV3; Allingham et al., 2005). The chiral OH groups of both inhibitors interact with the same residues Gly^{248} and Leu^{270} (Gly^{240} and Leu^{262} in *Dictyostelium*). Mesh, surfaces based on Van-der-Walls radii, calculated with PyMol. (Bottom) Residues involved in compound binding in Ligplot+ v2.2 (Laskowski and Swindells, 2011) representation are shown; U50, upper 50-kDa subdomain; L50, lower 50-kDa subdomain (gray); sw-2, switch-2 loop (red); HP, HP-helix (beige). Hydrogen bonds (up to 3.2 Å) are shown as green lines.

(C) MPH-220-bound MyHC IIb structure with superimposed cardiac HP-helix illustrates the steric clash between the morpholine ring of MPH-220 and the cardiac HP-helix Phe^{473} (red) residue.

See also Figure S3.

validated the *in silico* approach to design molecules for selective inhibitor development (Figure S3).

We further studied the effect of MPH-220 on muscle force generation in living animals (Figure 3A). In agreement with the ATPase inhibitory properties, the S(−) enantiomer of MPH-220 was drastically more effective than the R(+) enantiomer when animals were treated orally with MPH-220 (Figure S4). Consequently, the force-relaxing effect of the racemic mixture was significantly lower than that of the S(−) enantiomer. Although the racemic mixture caused maximum 40% reduction, the S(−) enantiomer could decrease hindleg force by 70% in a concentration-dependent manner (Figures 3B and 3C). The 30% residual isometric force level for S(−)-MPH-220 is in line with the presence of uninhibitable slow skeletal muscle isoforms in rat hindleg muscles. This attribute is of high importance because, unlike centrally acting muscle relaxants, MPH-220 would never cause overdose-related patient immobilization due to the remaining slow myosin-mediated muscle tone. Importantly, the decreased force persisted for more than 10 h (Figure 3C), which indicates optimal properties for pharmacological development. The force-relaxing effect after oral administration was only marginally slower than that after intraperitoneal injection (Figure S4), which

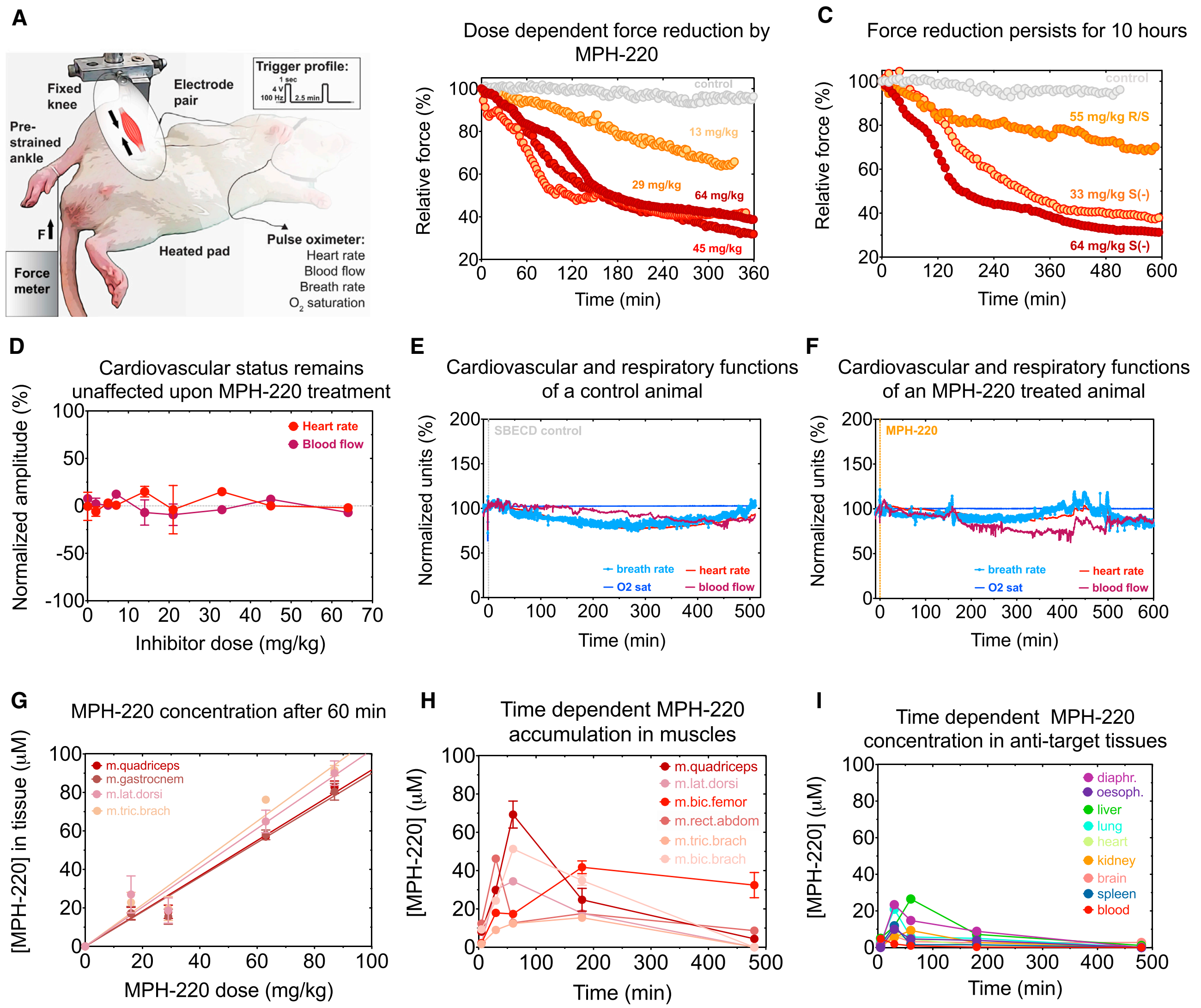

Figure 3. MPH-220 Reduces Skeletal Muscle Force without Cardiovascular Effects

(A) Isometric force of rat hindleg was measured while vital functions were detected by a non-invasive pulse oximeter.

(B and C) Dose-dependent force reduction after MPH-220 treatment persisted for more than 10 h.

(D) Heart rate (red circle) and pulse distention—reflecting local blood flow at the carotid artery—(maroon circle) show the maximal signal deflections during the measurements (60–600 min) on 1–4 animals/dose.

(E and F) Cardiovascular and respiratory functions as a function of time after treatment with sulfobutyl-ether-β-cyclodextrin (SBECD) control or MPH-220. Note that permanent oxygen level is maintained by O_2-supplemented isoflurane anesthesia.

(G) Dose-dependent MPH-220 accumulation in rat muscle tissues 60 min after oral treatment. Mean ± SD are shown; n = 2–3.

(H and I) Time-dependent MPH-220 accumulation in rat tissues after 35 mg/kg intraperitoneal (i.p.) treatment.

Mean ± SD are shown; n = 2–11. See also Figure S4.

indicated optimal absorption properties of MPH-220. High endothelial permeability was further confirmed by Caco-2 assay, which showed that MPH-220 is highly permeable with significantly faster transfer rate in the absorptive direction over the excretive direction (Figure S4).

Although skeletal muscle relaxation could be efficiently achieved by MPH-220, cardiac function was not perturbed in the concentration range that was effective in skeletal muscle force relaxation experiments (Figures 3F and S4). More importantly, neither cardiac nor respiratory functions differed significantly from the excipient control during the 10-h experiments, suggesting a reasonable safety range between the effective and toxic doses of MPH-220 (Figures 3E and 3F). The maximum 25% decrease in heart rate and blood flow parameters is most probably due to the 10-h-long anesthesia without food and drink after an overnight starvation period and not the effect of myosin inhibition (Figure S4). Moreover, the identical direction of the change in heart rate and blood flow parameters solely reflects

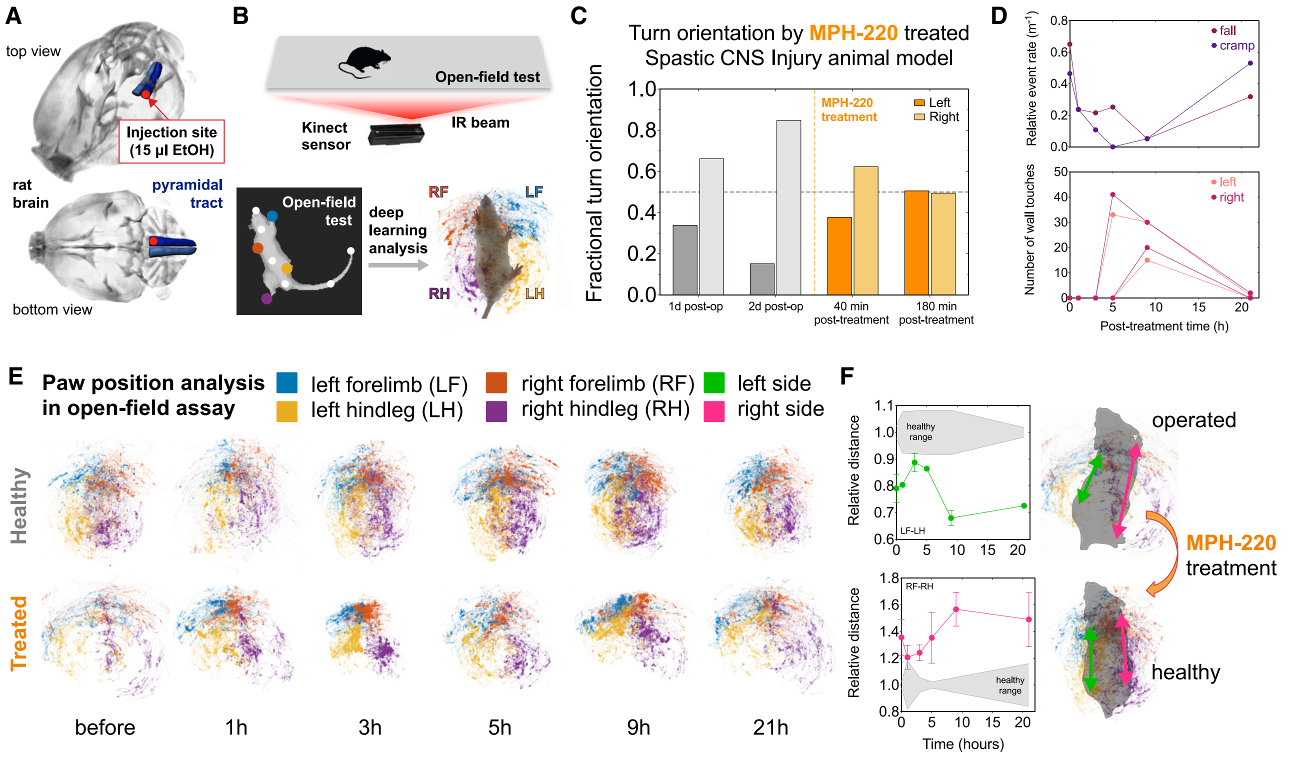

Figure 4. MPH-220 Efficiently Improves Gait Functions of Spastic Rats after Brain Injury

(A) Position of pyramidal tract lesion (red dots).

(B) Open-field gait analysis was performed by deep-learning algorithms coupled to sub-millimeter 3D movement detection. Dots represent the determined positions; right and left forelimbs (RF and LF) and right and left hindlegs (RH and LH).

(C) Fractional turn orientation of spastic rat before (gray) and after (orange) 15 mg/kg MPH-220 treatment.

(D) Falling and spontaneous cramping rates normalized to the total distance traveled (upper) and the number of touches on the cylinder wall (lower) after 20 mg/kg MPH-220 treatment.

(E) Paw position distribution of the healthy (upper) and treated (lower) animals before and after 20 mg/kg MPH-220 treatment in slow regime.

(F) Averaged distances between the left (upper) and right (lower) fore- and hindlimbs in each frame of the 3D recordings relative to the healthy values. Mean ± SD are shown.

See also Figure S5.

slowing down the heart during anesthesia, because cardiac myosin inhibition preceding heart failure increases heart rate while drastically lowering blood flow, as shown with the non-selective inhibitor, AmBleb (Figure S4).

We also examined MPH-220 distribution in rat tissues in a time-dependent manner and observed a dose-dependent, few-fold accumulation of MPH-220 in skeletal muscle samples over other tissues, including brain, heart, kidney, and blood (Figures 3G–3I). Accumulation in skeletal muscle persists after 3 h when MPH-220 is completely eliminated from blood and other tissues, whereas its concentration in target muscles is still in the effective concentration range (10-fold higher than the determined inhibitory constant [IC_{50}]). MPH-220 concentration was only temporarily elevated in the liver, which metabolizes MPH-220. We note that MPH-220 concentration in the diaphragm was much lower compared to other striated muscle samples, which explains the lack of respiratory dysfunctions after MPH-220 treatments. This feature is expected to prove even more favorable in human patients due to the substantially higher ratio of MyHC I slow isoforms in human diaphragm (Figure S1). The pronounced accumulation of MPH-220 in skeletal muscles might be the result of high concentration of fast skeletal myosin isoforms, which bind the inhibitor with high affinity. This hypothesis is supported by the significantly lower accumulation of the R(+) enantiomer, which further explains the 4-fold weaker force relaxation by the R(+) enantiomer (cf. Figure S4A). The species-specific MyHC distribution (Figure S1) also emphasizes the need for testing these pharmacodynamic properties of MPH-220 in larger animals (dogs and mini pigs), which—unlike rodents—have higher slow isoform proportions, more similar to human tissues.

Direct and efficient targeting of skeletal muscle contraction by MPH-220 raises the possibility of the development of a new-generation, nervous-system-independent, anti-spastic drug. Therefore, we investigated the efficiency of MPH-220 to improve spasticity-related gait disorders in rats with brain injury. We applied the recently developed spastic cerebral palsy animal model to provoke paralysis-coupled spasticity in rats (Figure 4A; Yu et al., 2013), and gait disorders were analyzed by non-invasive methods focusing on the motoric functions of rats combined with neural-network-based deep-learning movement analysis

(Figure 4B; Video S1). Similarly to human patients with stroke or brain trauma, rats showed individually variable gait patterns with different degrees of palsy in the lower limbs. Thus, we analyzed the effect of MPH-220 treatment individually on each animal and focused on treatment-induced changes in spasticity-related gait components.

Rat-A could not use the right forelimb and the left hindleg due to paralysis-coupled spasticity, which resulted in an almost complete one-sided circling behavior in the open-field box 2 days after the surgery (Video S2). 40 min after MPH-220 treatment, the ratio of left turns increased from 15% to 38%, which further improved to 51% 3 h after the treatment (Figure 4C). Even though rat-A walked significantly less after treatment, it was obvious that a major improvement was achieved: after relaxing spasticity in its left hindleg, rat-A was able to use this leg and make quasi-normal steps (Video S3). Rat-B and C also had paralysis-coupled spasticity in the hindlegs, although to a lower degree than rat-A. The most obvious spasticity-related feature in the open-field test was the random falling and the spontaneous cramping of the right hindleg of rat-C (Video S4). Importantly, the relative frequency of both symptoms decreased drastically after MPH-220 treatment (Figure 4D). Besides these serious gait abnormalities, rat-B and C could not stand up in the cylinder assay before MPH-220 treatment. In agreement with the kinetics observed in the open-field assay, 3 and 5 h after oral MPH-220 treatment, both rats could stand up in the cylinder, touching the wall with both forepaws with the same number of events as their healthy littermates (Figure 4D). Next morning, the positive effects on falling and cramping frequencies and on the ability to stand up in the cylinder disappeared as MPH-220 was excreted from their bodies. Rat-D showed spastic gait disorders only in the right hindleg without signs of severe palsy, and all other legs remained unaffected. This animal could not use the right hindleg normally due to stiff muscles, which resulted in abnormal positioning of all four paws (Figures 4E and S5). The spastic leg was offset from the body axis, which hindered normal progression of the limb during walking and resulted in lopsided gait patterns with tilted body axis (Figures 4F and S5; Video S5). After MPH-220 treatment, the gait of this animal improved significantly as it started to use both hindlegs normally. The improved movement was the consequence of relaxed spasticity in the hindlegs, which enabled the animal to pull its leg into the body axis, thereby making normal walking steps (Figures 4E, 4F, and S5; Video S5). The enhanced gait functions remained persistent for 5 h, when paw positions and body symmetry were close to those of the healthy animals. Similarly to the other experiments, the effect relapsed to the pretreatment state after 21 h. These effects could be reproduced 5 and 12 days after the first treatment, corroborating the specific anti-spastic effect of MPH-220 treatment.

Beside the individual patterns of spastic behavior that could be improved by MPH-220 treatment, deep-learning analysis was used to assess the over-ground locomotion of all animals during 15 min of free movement in the open-field test. We used 28 parameters characterizing the 3D position of the limbs and body axis in three movement-speed regimes (Figure S5) to quantify the locomotor features based on pose-estimating deep-learning algorithms and exposed these to a principal-components analysis (PCA). In the global PCA space—including all three speed regimes—the major gait component (PC1) was significantly different from the healthy range, indicating that pyramidal tract damage-induced spastic walk asymmetry is reflected in the major principal gait component (Figure 5A). Most importantly, MPH-220 treatment significantly decreased PC1 scores, the effect of which was maximal at 3 h and no longer detected after 21 h. Importantly, PC1 scores were significantly different from the untreated level, however, the treated values did not differ significantly from the healthy range, which confirms that MPH-220 ameliorated gait pattern of the treated animals to that of the healthy rats. However, when we analyzed the three speed regimes separately, we found that pyramid tract damage mostly affected PC1 in the slow and medium-speed regimes, whereas PC2 and PC3 were significantly affected in the fast regime (Figures 5B and S5). More importantly, PC1 could be significantly improved by MPH-220 treatment in the slow- and medium-speed regimes, and PC3 was significantly improved in the fast regime. We identified the major parameters that predominantly contributed to PC1 and PC3 in the slow, medium, and fast regimes and found a marked difference in the parameter sets defining PC1 and PC3 (Figures 5C, 5D, and S5). Analysis of these components revealed that, in the slow- and medium-speed regimes, MPH-220 treatment has the largest effect on the volumes of the ellipsoids representing paw positions and on the distances between their centers, both suggesting a much-ordered stepping pattern and straightened body axis (Figure 5E). On the other hand, in the fast regime, MPH-220 has the most pronounced effect on the angles of the ellipsoids, which indicates that the treated rats could keep their legs closer to the body axis similarly to the healthy running pattern. These results further solidify that MPH-220 is capable of treating the spastic component of movement abnormalities after brain injury, exhibiting a promising potential to address the unmet medical need for effective anti-spastic therapies.

DISCUSSION

Our biochemical and *in vivo* results demonstrate that MPH-220 selectively inhibits fast skeletal myosin-2 isoforms, which enables effective improvements of spastic gait disorders after brain damage as a consequence of efficient reduction of muscle force. These findings emphasize that nervous-system-injury-derived muscle spasticity can be treated by directly targeting the effector protein of muscle contraction, thereby avoiding adverse neurological and cardiovascular side effects that are characteristic of currently used muscle relaxants. Moreover, as MPH-220 proved a promising candidate for further anti-spastic drug development, we tested its pharmacological properties by investigating its off-target effects on human enzymes, including kinase panels and G-protein-coupled and nuclear hormone receptors (Figure S6). We also demonstrate that MPH-220 is not mutagenic and not cytotoxic (Figure S6), which, together with its high-absorption properties, confirms that MPH-220 is safe and possesses optimal attributes for further drug development as a new-generation anti-spastic drug candidate.

Although we acknowledge that MPH-220 may cause general muscle weakness as observed in our animal disease model, we believe that this effect will be significantly less

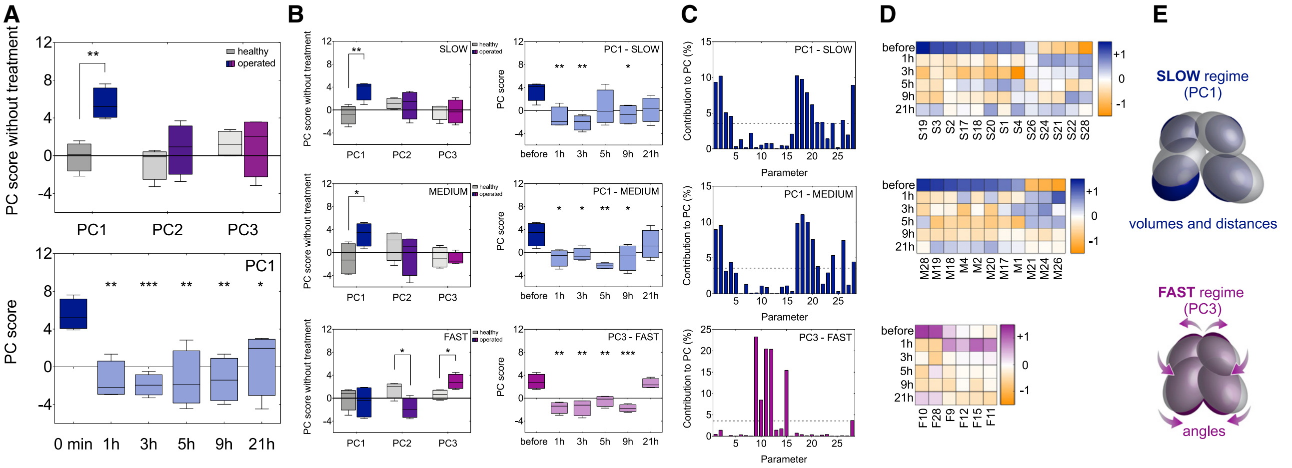

Figure 5. Principal-Component Analysis of Spastic Rats Reveals Details of Improved Gait Components after MPH-220 Treatment

(A and B) Box and whiskers (min to max) representation of global (A) and speed-specific (B) principal-component (PC) analysis of gait parameters of healthy (gray) and operated (colored) animals before (darker) and after (lighter) MPH-220 treatment.

(C) Parameter contributions to PC1 in the slow and medium regimes and to PC3 in the fast regimes (cf. Figure S5).

(D) Heatmap of major parameters contributing to PC1 (blue-orange) and PC3 (purple-orange; cf. Figure S5).

(E) Schematic representation of MPH-220 effects on paw positions in slow and fast regimes.

See also Figure S5.

pronounced in human patients due to the higher ratio of MyHC I slow skeletal muscle myosin isoform. In human skeletal muscles, the presence of 40%–60% MyHC I isoform, which is not inhibited by MPH-220, highlights another important aspect of this type of muscle relaxation as opposed to nervous-system-targeting medications. Although general weakness of aspecific muscle groups may appear by using both types of muscle relaxants, the MPH-220-based anti-spastic effect is not expected to cause complete immobilization of patients due to the residual muscle tone from the uninhibited slow isoform fraction. Another concern may arise regarding extraocular muscles, which express MYH13 gene product containing Leu required for MPH-220 inhibition (Figure S1). Nevertheless, in adult human extraocular muscles, significant amount of α-cardiac myosin heavy chain is expressed (Kjellgren et al., 2003); therefore, these muscles will also not be completely immobilized by MPH-220. However, these effects might be investigated during future clinical trials. Moreover, based on the complex pathophysiology of spasticity development (Trompetto et al., 2014), we suppose that early treatment with an effective anti-spastic drug will significantly delay the onset and markedly reduce the severity of spastic symptoms after nervous system injuries.

Besides traumatic brain and spinal cord injuries in stroke and cerebral palsy, spasticity is also a common symptom in several other diseases of broad etiology (Table 1). Spasticity is a major component of upper motor neuron lesion syndromes, including multiple sclerosis, amyotrophic lateral sclerosis, spastic paraplegia, multiple system atrophy, and atypical Parkinsonism, and also a characteristic symptom in several skeletal muscle myopathies, such as myotonia congenita, myotonia fluctuans, or certain neurodegenerative diseases. Altogether, spasticity in these syndromes affect nearly 1% of the human population (cca. 55 million spastic patients), and more than 10% of people suffer from often-painful muscle stiffness in low back pain and fibromyalgia (Marques et al., 2017; Vos et al., 2012). Consequently, a nervous-system-independent, safe, and effective treatment is a significant unmet need from both clinical and socio-economical perspectives. Therefore, MPH-220 is a promising anti-spastic drug candidate to improve quality of life and may contribute to extended life expectancy (Blair et al., 2019; Gillard et al., 2015; Slaman et al., 2014; Yi et al., 2019) of these patients and would provide new therapeutic protocols for clinicians in these diverse indications.

STAR★METHODS

Detailed methods are provided in the online version of this paper and include the following:

- KEY RESOURCES TABLE
- RESOURCE AVAILABILITY
  - ○ Lead Contact
  - ○ Materials Availability
  - ○ Data and Code Availability
- EXPERIMENTAL MODEL AND SUBJECT DETAILS
  - ○ Animals
  - ○ Human muscle biopsies
- METHOD DETAILS
  - ○ Materials
  - ○ Proteins
  - ○ ATPase measurement
  - ○ Molecular dynamics simulation
  - ○ Crystallization and data processing
  - ○ Structure determination and refinement

Table 1. Prevalence of Diseases with Broad Etiologies in which Muscle Spasticity Is One of the Major Characteristic Symptoms

Disease	Background	Symptom	Prevalence (per 100,000)	Patient Number	Ratio of Spasticity
Stroke	blood flow disruption in the brain either by a blood clot or by hemorrhage	weakness, paralysis, spasticity, coordination and balance problems, memory problems	100–600 (Kim et al., 2015; Yi et al., 2020)	30 million	38%–46% (Lundström et al., 2008; Opheim et al., 2014; Urban et al., 2010; Wissel et al., 2013; 11–14 million spastic patients)
Multiple sclerosis (MS)	autoimmune disease attacking the myelin sheaths of nerve fibers	fatigue, gait difficulties, numbness, spasticity, weakness, vision problems	300–400 in US (Wallin et al., 2019)	2.3 million	50%[a] (1.5–2 million spastic patients)
Cerebral palsy (CP)	brain development disorders or disruption, due to genetic mutations, infections, trauma, or injury	muscle stiffness, spasticity, ataxia, tremors, gait disorders	150–300 (Kruse et al., 2009; Pulgar et al., 2019; Van Naarden Braun et al., 2016)	17 million	70%–75% (Novak, 2014; Pulgar et al., 2019; 12 to 13 million spastic patients)
Amyotrophic lateral sclerosis (ALS)	degeneration of cortical motor neurons, the motor nuclei of the brainstem, and the anterior horn cells of the spinal cord	muscle weakness, atrophy, spasticity	4 to 5 (Xu et al., 2020)	14–15,000 (US)[b]	40% (Meyer et al., 2019; 6,000 spastic patients)
Traumatic brain injury (TBI)	blow or jolt to the head or a head injury that disrupts normal functions	paralysis, sensory impairments, headaches, coordination, spasticity	1% (up to 15%; Dewan et al., 2018), 475,000 children/year (US; Enslin et al., 2020)	1.7–2 million new TBI/year in US (Enslin et al., 2020), 68–71 million worldwide (Dewan et al., 2018)	5%–19% (Bose et al., 2015; Verplancke et al., 2005; 30–35 million spastic patients)
Multiple system atrophy (MSA)	progressive neurodegenerative disease with alpha-synuclein accumulation in glia (form of atypical Parkinsonism)	slow movement, muscle stiffness, spasticity, incoordination, tremors, bladder control problems	2–6 (Bjornsdottir et al., 2013)		
Spastic paraplegia	defects in transport of proteins, lipids through long nerve fibers (axons)	progressive gait disorder, spasticity	3–6		
Myotonia congenita (Becker disease)	abnormality of skeletal muscle membranes resulting in hyperexcitability	painless spasm, difficulty relaxing muscles (myotonia), rigidity, abnormally enlarged muscles (hypertrophy)	1 to 2 (Romitti et al., 2015)		
Spinal cord injury or tumors	nerve damage due to, e.g., thoracic spine herniated discs damage the nerves	pain, increased reflexes in legs that can cause spasticity, muscle weakness, numbness or tingling	2–8 (Witiw and Fehlings, 2015)		

[a] WHO Atlas multiple sclerosis resources in the world 2008 (http://www.who.int/mental_health/neurology)
[b] NIH amyotrophic lateral sclerosis (ALS) brochure (https://www.ninds.nih.gov/Disorders)

  - ○ Isometric force measurement
  - ○ Non-invasive measurement of cardiovascular and respiratory functions
  - ○ Concentration measurement from tissue samples
  - ○ Spasticity animal model
  - ○ Neural network based deep-learning analysis of movements in open-field tests
  - ○ Cylinder assay
  - ○ Safety panel measurements
- QUANTIFICATION AND STATISTICAL ANALYSIS

SUPPLEMENTAL INFORMATION

Supplemental Information can be found online at https://doi.org/10.1016/j.cell.2020.08.050.

ACKNOWLEDGMENTS

We would like to thank Prof. Árpád Dobolyi for help in rat operations; Máté Winternitz, Noémi Karnok, Kinga Oravecz, and Henrietta Hóf for technical assistance; and beam line scientists of PX2A (SOLEIL synchrotron) for excellent support during data collection. We also thank Prof. James R. Sellers (NIH-NHLBI), Ádám Miklósi (ELTE), and Csaba Szalontai (ELTE) for detailed discussions and helpful comments on the manuscript and Prof. Matthias Preller (MHH) for helpful discussions regarding MD simulations. This study has been supported by the Hungarian National Research, Development and Innovation Office (NVKP 16-1-2016-0051 to M.G., A.Á.R., and A.M.-C.) and the Hungarian Ministry of Finance (GINOP-2.1.7-15-2016-02580 to M.G. and A.Á.R.). L.C. is the recipient of a PhD fellowship from Ligue Contre le Cancer IP/SC-16058. A.H. was supported by grants from CNRS, FRM DCM20181039553, ANR-17-CE11-0029-01, and AFM 21805. The A.H. team is part of the Labex CelTisPhyBio:11-LBX-0038, which is part of the IDEX PSL (ANR-10-IDEX-0001–02 PSL). D.V.T., K.M.R., and J.A.S. are supported by National Institutes of Health grants R01 GM033289 and R01 HL1171138. D.V.T. is supported by an American Heart Association postdoctoral fellowship (17POST33411070).

AUTHOR CONTRIBUTIONS

Conceptualization, M.G., S.K., and A.M.-C.; Formal Analysis, M.G., Á.I.H., D.T., S.K.S., C. Kurdi, L.C., C. Kikuti, I.L., A.H., and A.M.-C.; Funding Acquisition, M.G., J.A.S., A.Á.R., M.K., S.K., and A.M.-C.; Investigation, M.G., Á.I.H., D.T., S.K.S., M.P., C. Kurdi, L.C., C. Kikuti, K.M.R., D.V.T., I.L., E.P., and A.M.-C.; Methodology Development, M.G., M.P., L.C., C. Kikuti., I.L., A.H., and A.M.-C.; Supervision, M.G., M.K., and A.M.-C.; Validation, M.G., Á.I.H., D.T., and A.M.-C.; Visualization, M.G. and A.M.-C.; Writing, M.G. and A.M.-C.; Software Development, D.T.; Crystallization and Structure Determination, L.C.; Structure Refinement, C. Kikuti.; Preparation of Human Cardiac Myosin Sample, K.M.R. and D.V.T.; Supervision for Human Cardiac Myosin Sample, J.A.S.; Writing – Review & Editing, A.Á.R. and M.K.; Funding Acquisition for Crystallization and Structure Determination, A.H.

DECLARATION OF INTERESTS

The authors declare the following competing interests: employment, A.M.-C. and M.G. are owners of Motorpharma, Ltd. and A.Á.R. and M.G. are part-time employed by Motorpharma, Ltd.; related patents, PCT/EP2017/051829, WO/2017/129782, HU1800129A2, PCT/HU2019/050017, WO/2019/202346A2, and WO/2019/202346A3; J.A.S. is a cofounder and member of the scientific advisory boards of Cytokinetics and MyoKardia, biotechnology companies developing small molecules that target the sarcomere for the treatment of various muscle diseases; K.M.R. is on the scientific advisory board at MyoKardia; and J.A.S., D.V.T., and K.M.R. are cofounders of Kainomyx Inc., a biotechnology company focused on developing small molecules to target tropical diseases.

Received: May 23, 2020
Revised: July 24, 2020
Accepted: August 27, 2020
Published: October 8, 2020

SUPPORTING CITATIONS

The following references appear in the Supplemental Information: Billington et al. (2013); Várkuti et al., 2016; Kovács et al. (2003); Wang et al. (2003); Zhang et al. (2017).

REFERENCES

Allingham, J.S., Smith, R., and Rayment, I. (2005). The structural basis of blebbistatin inhibition and specificity for myosin II. Nat. Struct. Mol. Biol. *12*, 378–379.

Berman, H., Henrick, K., and Nakamura, H. (2003). Announcing the worldwide Protein Data Bank. Nat. Struct. Biol. *10*, 980.

Billington, N., Wang, A., Mao, J., Adelstein, R.S., and Sellers, J.R. (2013). Characterization of three full-length human nonmuscle myosin II paralogs. J. Biol. Chem. *288*, 33398–33410.

Bjornsdottir, A., Gudmundsson, G., Blondal, H., and Olafsson, E. (2013). Incidence and prevalence of multiple system atrophy: a nationwide study in Iceland. J. Neurol. Neurosurg. Psychiatry *84*, 136–140.

Blair, E., Langdon, K., McIntyre, S., Lawrence, D., and Watson, L. (2019). Survival and mortality in cerebral palsy: observations to the sixth decade from a data linkage study of a total population register and National Death Index. BMC Neurol. *19*, 111.

Bose, P., Hou, J., and Thompson, F.J. (2015). Traumatic brain injury (TBI)-induced spasticity: neurobiology, treatment, and rehabilitation. In Brain Neurotrauma: Molecular, Neuropsychological, and Rehabilitation Aspects, F.H. Kobeissy, ed. (CRC).

Bricogne, G., Blanc, E., Brandl, M., Flensburg, C., Keller, P., Paciorek, W., Roversi, P., Sharff, A., Smart, O.S., Vonrhein, C., et al. (2017). BUSTER version 2.10.3 (Global Phasing).

Careta, M.F., Delgado, L., and Patriota, R. (2015). Report of allergic reaction after application of botulinum toxin. Aesthet. Surg. J. *35*, NP102–NP105.

Coluccio, L.M. (2020). Myosins and disease. Adv. Exp. Med. Biol. *1239*, 245–316.

Cope, M.J., Whisstock, J., Rayment, I., and Kendrick-Jones, J. (1996). Conservation within the myosin motor domain: implications for structure and function. Structure *4*, 969–987.

Dewan, M.C., Rattani, A., Gupta, S., Baticulon, R.E., Hung, Y., Punchak, M., Agrawal, A., Adeleye, A.O., Shrime, M.G., Rubiano, A.M., et al. (2018). Estimating the global incidence of traumatic brain injury. J. Neurosurg. *130*, 1080–1097.

Emsley, P., and Cowtan, K. (2004). Coot: model-building tools for molecular graphics. Acta Crystallogr. D Biol. Crystallogr. *60*, 2126–2132.

England, J., and Loughna, S. (2013). Heavy and light roles: myosin in the morphogenesis of the heart. Cell. Mol. Life Sci. *70*, 1221–1239.

Enslin, J.M.N., Rohlwink, U.K., and Figaji, A. (2020). Management of spasticity after traumatic brain injury in children. Front. Neurol. *11*, 126.

Gillard, P.J., Sucharew, H., Kleindorfer, D., Belagaje, S., Varon, S., Alwell, K., Moomaw, C.J., Woo, D., Khatri, P., Flaherty, M.L., et al. (2015). The negative impact of spasticity on the health-related quality of life of stroke survivors: a longitudinal cohort study. Health Qual. Life Outcomes *13*, 159.

Gotoh, T., Miyazaki, Y., Sato, W., Kikuchi, K., and Bentley, W.E. (2001). Proteolytic activity and recombinant protein production in virus-infected Sf-9 insect cell cultures supplemented with carboxyl and cysteine protease inhibitors. J. Biosci. Bioeng. *92*, 248–255.

Gourinath, S., Himmel, D.M., Brown, J.H., Reshetnikova, L., Szent-Györgyi, A.G., and Cohen, C. (2003). Crystal structure of scallop Myosin s1 in the pre-power stroke state to 2.6 a resolution: flexibility and function in the head. Structure *11*, 1621–1627.

Gyimesi, M., Kintses, B., Bodor, A., Perczel, A., Fischer, S., Bagshaw, C.R., and Málnási-Csizmadia, A. (2008). The mechanism of the reverse recovery step, phosphate release, and actin activation of Dictyostelium myosin II. J. Biol. Chem. *283*, 8153–8163.

Heissler, S.M., and Manstein, D.J. (2011). Comparative kinetic and functional characterization of the motor domains of human nonmuscle myosin-2C isoforms. J. Biol. Chem. *286*, 21191–21202.

Kawana, M., Sarkar, S.S., Sutton, S., Ruppel, K.M., and Spudich, J.A. (2017). Biophysical properties of human β-cardiac myosin with converter mutations that cause hypertrophic cardiomyopathy. Sci. Adv. *3*, e1601959.

Kim, A.S., Cahill, E., and Cheng, N.T. (2015). Global stroke belt: geographic variation in stroke burden worldwide. Stroke *46*, 3564–3570.

Kjellgren, D., Thornell, L.E., Andersen, J., and Pedrosa-Domellöf, F. (2003). Myosin heavy chain isoforms in human extraocular muscles. Invest. Ophthalmol. Vis. Sci. *44*, 1419–1425.

Kovács, M., Wang, F., Hu, A., Zhang, Y., and Sellers, J.R. (2003). Functional divergence of human cytoplasmic myosin II: kinetic characterization of the non-muscle IIA isoform. J. Biol. Chem. *278*, 38132–38140.

Kovács, M., Tóth, J., Hetényi, C., Málnási-Csizmadia, A., and Sellers, J.R. (2004). Mechanism of blebbistatin inhibition of myosin II. J. Biol. Chem. *279*, 35557–35563.

Kruse, M., Michelsen, S.I., Flachs, E.M., Brønnum-Hansen, H., Madsen, M., and Uldall, P. (2009). Lifetime costs of cerebral palsy. Dev. Med. Child Neurol. *51*, 622–628.

Laskowski, R.A., and Swindells, M.B. (2011). LigPlot+: multiple ligand-protein interaction diagrams for drug discovery. J. Chem. Inf. Model. *51*, 2778–2786.

Li, S. (2017). Spasticity, motor recovery, and neural plasticity after stroke. Front. Neurol. *8*, 120.

Limouze, J., Straight, A.F., Mitchison, T., and Sellers, J.R. (2004). Specificity of blebbistatin, an inhibitor of myosin II. J. Muscle Res. Cell Motil. *25*, 337–341.

Lundström, E., Terént, A., and Borg, J. (2008). Prevalence of disabling spasticity 1 year after first-ever stroke. Eur. J. Neurol. *15*, 533–539.

Maier, J.A., Martinez, C., Kasavajhala, K., Wickstrom, L., Hauser, K.E., and Simmerling, C. (2015). ff14SB: improving the accuracy of protein side chain and backbone parameters from ff99SB. J. Chem. Theory Comput. *11*, 3696–3713.

Málnási-Csizmadia, A., and Kovács, M. (2010). Emerging complex pathways of the actomyosin powerstroke. Trends Biochem. Sci. *35*, 684–690.

Margossian, S.S., and Lowey, S. (1982). Preparation of myosin and its subfragments from rabbit skeletal muscle. Methods Enzymol. *85*, 55–71.

Marques, A.P., Santo, A.S.D.E., Berssaneti, A.A., Matsutani, L.A., and Yuan, S.L.K. (2017). Prevalence of fibromyalgia: literature review update. Rev. Bras. Reumatol. Engl. *57*, 356–363.

Martin, A., Abogunrin, S., Kurth, H., and Dinet, J. (2014). Epidemiological, humanistic, and economic burden of illness of lower limb spasticity in adults: a systematic review. Neuropsychiatr. Dis. Treat. *10*, 111–122.

Mathis, A., Mamidanna, P., Cury, K.M., Abe, T., Murthy, V.N., Mathis, M.W., and Bethge, M. (2018). DeepLabCut: markerless pose estimation of user-defined body parts with deep learning. Nat. Neurosci. *21*, 1281–1289.

McCoy, A.J., Grosse-Kunstleve, R.W., Adams, P.D., Winn, M.D., Storoni, L.C., and Read, R.J. (2007). Phaser crystallographic software. J. Appl. Cryst. *40*, 658–674.

Medical Advisory, S.; Medical Advisory Secretariat (2005). Intrathecal baclofen pump for spasticity: an evidence-based analysis. Ont. Health Technol. Assess. Ser. *5*, 1–93.

Meleger, A.L. (2006). Muscle relaxants and antispasticity agents. Phys. Med. Rehabil. Clin. N. Am. *17*, 401–413.

Meyer, T., Funke, A., Münch, C., Kettemann, D., Maier, A., Walter, B., Thomas, A., and Spittel, S. (2019). Real world experience of patients with amyotrophic lateral sclerosis (ALS) in the treatment of spasticity using tetrahydrocannabinol:cannabidiol (THC:CBD). BMC Neurol. *19*, 222.

Miyata, S., Minobe, W., Bristow, M.R., and Leinwand, L.A. (2000). Myosin heavy chain isoform expression in the failing and nonfailing human heart. Circ. Res. *86*, 386–390.

Mukherjee, A., and Chakravarty, A. (2010). Spasticity mechanisms - for the clinician. Front. Neurol. *1*, 149.

Nath, T., Mathis, A., Chen, A.C., Patel, A., Bethge, M., and Mathis, M.W. (2019). Using DeepLabCut for 3D markerless pose estimation across species and behaviors. Nat. Protoc. *14*, 2152–2176.

NIH (2012). Dantrolene. In LiverTox: Clinical and Research Information on Drug-Induced Liver Injury (National Institute of Diabetes and Digestive and Kidney Diseases).

Novak, I. (2014). Evidence-based diagnosis, health care, and rehabilitation for children with cerebral palsy. J. Child Neurol. *29*, 1141–1156.

Opheim, A., Danielsson, A., Alt Murphy, M., Persson, H.C., and Sunnerhagen, K.S. (2014). Upper-limb spasticity during the first year after stroke: stroke arm longitudinal study at the University of Gothenburg. Am. J. Phys. Med. Rehabil. *93*, 884–896.

Orsnes, G.B., Sørensen, P.S., Larsen, T.K., and Ravnborg, M. (2000). Effect of baclofen on gait in spastic MS patients. Acta Neurol. Scand. *101*, 244–248.

Pavone, V., Testa, G., Restivo, D.A., Cannavò, L., Condorelli, G., Portinaro, N.M., and Sessa, G. (2016). Botulinum toxin treatment for limb spasticity in childhood cerebral palsy. Front. Pharmacol. *7*, 29.

Paxinos, G., and Watson, C. (2007). The Rat Brain in Stereotaxic Coordinates, Sixth Edition (Academic/Elsevier).

Planelles-Herrero, V.J., Hartman, J.J., Robert-Paganin, J., Malik, F.I., and Houdusse, A. (2017). Mechanistic and structural basis for activation of cardiac myosin force production by omecamtiv mecarbil. Nat. Commun. *8*, 190.

Pollard, C.E., Abi Gerges, N., Bridgland-Taylor, M.H., Easter, A., Hammond, T.G., and Valentin, J.P. (2010). An introduction to QT interval prolongation and non-clinical approaches to assessing and reducing risk. Br. J. Pharmacol. *159*, 12–21.

Pratt, S.J.P., and Lovering, R.M. (2014). A stepwise procedure to test contractility and susceptibility to injury for the rodent quadriceps muscle. J. Biol. Methods *1*, e8.

Pulgar, S., Bains, S., Gooch, J., Chambers, H., Noritz, G.H., Wright, E., Sawhney, T.G., Pyenson, B., and Ferro, C. (2019). Prevalence, patterns, and cost of care for children with cerebral palsy enrolled in Medicaid managed care. J. Manag. Care Spec. Pharm. *25*, 817–822.

Romitti, P.A., Zhu, Y., Puzhankara, S., James, K.A., Nabukera, S.K., Zamba, G.K., Ciafaloni, E., Cunniff, C., Druschel, C.M., Mathews, K.D., et al.; MD STARnet (2015). Prevalence of Duchenne and Becker muscular dystrophies in the United States. Pediatrics *135*, 513–521.

Rychlik, R., Kreimendahl, F., Schnur, N., Lambert-Baumann, J., and Dressler, D. (2016). Quality of life and costs of spasticity treatment in German stroke patients. Health Econ. Rev. *6*, 27.

Seidel, J.C. (1980). Fragmentation of gizzard myosin by alpha-chymotrypsin and papain, the effects on ATPase activity, and the interaction with actin. J. Biol. Chem. *255*, 4355–4361.

Slaman, J., Roebroeck, M., van der Slot, W., Twisk, J., Wensink, A., Stam, H., and van den Berg-Emons, R.; LEARN 2 MOVE Research Group (2014). Can a lifestyle intervention improve physical fitness in adolescents and young adults with spastic cerebral palsy? A randomized controlled trial. Arch. Phys. Med. Rehabil. *95*, 1646–1655.

Smit, C.A., and Slim, E.J. (2008). Heart conduction problems in a tetraplegic patient caused by a single therapeutic dosage of Baclofen. Spinal Cord *46*, 317–318.

Sommese, R.F., Sung, J., Nag, S., Sutton, S., Deacon, J.C., Choe, E., Leinwand, L.A., Ruppel, K., and Spudich, J.A. (2013). Molecular consequences of the R453C hypertrophic cardiomyopathy mutation on human β-cardiac myosin motor function. Proc. Natl. Acad. Sci. USA *110*, 12607–12612.

Spudich, J.A., and Watt, S. (1971). The regulation of rabbit skeletal muscle contraction. I. Biochemical studies of the interaction of the tropomyosin-troponin complex with actin and the proteolytic fragments of myosin. J. Biol. Chem. *246*, 4866–4871.

Straight, A.F., Cheung, A., Limouze, J., Chen, I., Westwood, N.J., Sellers, J.R., and Mitchison, T.J. (2003). Dissecting temporal and spatial control of cytokinesis with a myosin II Inhibitor. Science *299*, 1743–1747.

Sweeney, H.L., and Hammers, D.W. (2018). Muscle contraction. Cold Spring Harb. Perspect. Biol. *10*, a023200.

Takács, B., Billington, N., Gyimesi, M., Kintses, B., Málnási-Csizmadia, A., Knight, P.J., and Kovács, M. (2010). Myosin complexed with ADP and blebbistatin reversibly adopts a conformation resembling the start point of the working stroke. Proc. Natl. Acad. Sci. USA *107*, 6799–6804.

Tofferi, J.K., Jackson, J.L., and O'Malley, P.G. (2004). Treatment of fibromyalgia with cyclobenzaprine: A meta-analysis. Arthritis Rheum. *51*, 9–13.

Tong, C.W., Stelzer, J.E., Greaser, M.L., Powers, P.A., and Moss, R.L. (2008). Acceleration of crossbridge kinetics by protein kinase A phosphorylation of cardiac myosin binding protein C modulates cardiac function. Circ. Res. *103*, 974–982.

Trompetto, C., Marinelli, L., Mori, L., Pelosin, E., Currà, A., Molfetta, L., and Abbruzzese, G. (2014). Pathophysiology of spasticity: implications for neurorehabilitation. BioMed Res. Int. *2014*, 354906.

Trybus, K.M. (2000). Biochemical studies of myosin. Methods *22*, 327–335.

Urban, P.P., Wolf, T., Uebele, M., Marx, J.J., Vogt, T., Stoeter, P., Bauermann, T., Weibrich, C., Vucurevic, G.D., Schneider, A., and Wissel, J. (2010). Occurrence and clinical predictors of spasticity after ischemic stroke. Stroke *41*, 2016–2020.

Vagin, A., and Teplyakov, A. (2010). Molecular replacement with MOLREP. Acta Crystallogr. D Biol. Crystallogr. *66*, 22–25.

Van Naarden Braun, K., Doernberg, N., Schieve, L., Christensen, D., Goodman, A., and Yeargin-Allsopp, M. (2016). Birth prevalence of cerebral palsy: a population-based study. Pediatrics *137*, 1–9.

van Tulder, M.W., Touray, T., Furlan, A.D., Solway, S., and Bouter, L.M. (2003). Muscle relaxants for non-specific low back pain. Cochrane Database Syst. Rev. (2), CD004252.

Várkuti, B., H., Képiró, M., Horváth, I., Á., Végner, L., Ráti, S., Zsigmond, Á., Hegyi, G., Lenkei, Z., Varga, M., and Málnási-Csizmadia, A. (2016). A highly soluble, non-phototoxic, non-fluorescent blebbistatin derivative. Scientific Reports *6*, 26141.

Verplancke, D., Snape, S., Salisbury, C.F., Jones, P.W., and Ward, A.B. (2005). A randomized controlled trial of botulinum toxin on lower limb spasticity following acute acquired severe brain injury. Clin. Rehabil. *19*, 117–125.

Vonrhein, C., Flensburg, C., Keller, P., Sharff, A., Smart, O., Paciorek, W., Womack, T., and Bricogne, G. (2011). Data processing and analysis with the autoPROC toolbox. Acta Crystallogr. D Biol. Crystallogr. *67*, 293–302.

Vos, T., Flaxman, A.D., Naghavi, M., Lozano, R., Michaud, C., Ezzati, M., Shibuya, K., Salomon, J.A., Abdalla, S., Aboyans, V., et al. (2012). Years lived with disability (YLDs) for 1160 sequelae of 289 diseases and injuries 1990-2010: a systematic analysis for the Global Burden of Disease Study 2010. Lancet *380*, 2163–2196.

Wallin, M.T., Culpepper, W.J., Campbell, J.D., Nelson, L.M., Langer-Gould, A., Marrie, R.A., Cutter, G.R., Kaye, W.E., Wagner, L., Tremlett, H., et al.; US Multiple Sclerosis Prevalence Workgroup (2019). The prevalence of MS in the United States: a population-based estimate using health claims data. Neurology *92*, e1029–e1040.

Wang, F., Kovacs, M., Hu, A., Limouze, J., Harvey, E.V., and Sellers, J.R. (2003). Kinetic mechanism of non-muscle myosin IIB: functional adaptations for tension generation and maintenance. J. Biol. Chem. *278*, 27439–27448.

Wang, J., Wolf, R.M., Caldwell, J.W., Kollman, P.A., and Case, D.A. (2004). Development and testing of a general amber force field. J. Comput. Chem. *25*, 1157–1174.

Waterhouse, A., Bertoni, M., Bienert, S., Studer, G., Tauriello, G., Gumienny, R., Heer, F.T., de Beer, T.A.P., Rempfer, C., Bordoli, L., et al. (2018). SWISS-MODEL: homology modelling of protein structures and complexes. Nucleic Acids Res. *46* (W1), W296–W303.

Wissel, J., Manack, A., and Brainin, M. (2013). Toward an epidemiology of poststroke spasticity. Neurology *80* (3, Suppl 2), S13–S19.

Witiw, C.D., and Fehlings, M.G. (2015). Acute spinal cord injury. J. Spinal Disord. Tech. *28*, 202–210.

Xu, L., Liu, T., Liu, L., Yao, X., Chen, L., Fan, D., Zhan, S., and Wang, S. (2020). Global variation in prevalence and incidence of amyotrophic lateral sclerosis: a systematic review and meta-analysis. J. Neurol. *267*, 944–953.

Yi, Y.G., Jung, S.H., and Bang, M.S. (2019). Emerging issues in cerebral palsy associated with aging: a physiatrist perspective. Ann. Rehabil. Med. *43*, 241–249.

Yi, X., Luo, H., Zhou, J., Yu, M., Chen, X., Tan, L., Wei, W., and Li, J. (2020). Prevalence of stroke and stroke related risk factors: a population based cross sectional survey in southwestern China. BMC Neurol. *20*, 5.

Yu, Y., Li, L., Shao, X., Tian, F., and Sun, Q. (2013). Establishing a rat model of spastic cerebral palsy by targeted ethanol injection. Neural Regen. Res. *8*, 3255–3262.

Zhang, Y., Li, L., Zhao, Y., Han, H., Hu, Y., Liang, D., Yu, B., and Kou, J. (2017). The myosin II inhibitor, blebbistatin, ameliorates FeCl3-induced arterial thrombosis via the GSK3β-NF-κB pathway. Int. J. Biol. Sci. *13*, 630–639.

Zorowitz, R.D., Gillard, P.J., and Brainin, M. (2013). Poststroke spasticity: sequelae and burden on stroke survivors and caregivers. Neurology *80* (3, Suppl 2), S45–S52.

STAR★METHODS

KEY RESOURCES TABLE

REAGENT or RESOURCE	SOURCE	IDENTIFIER
Bacterial Strains		
Salmonella typhimurium TA98 (*hisD3052*)	Xenometrix AG	Cat# A10-210
Salmonella typhimurium TA100 (*hisG46*)	Xenometrix AG	Cat# A10-210
Biological Samples		
Lyophilized rat liver S9, Phenobarbital/β-Naphtoflavone induced	Xenometrix AG	Cat# A10-210-S2-P
Adult Human Left Ventricular tissue sample	AnaBios Corporation	Cat# Car-148/F
Adult Human Muscle Biopsies	This paper, University of Pécs	N/A
Critical Commercial Assays		
gpcrMAX	DiscoverX® Profiling service, Eurofins	Cat# 86-0115
Caco-2	Absorption and Permeability Services, Eurofins Discovery	Cat# 4560, 4561, 4482, 4483
Predictor^{TM} hERG Fluroescence Polarization Assay	SelectScreen Profiling, Thermo Fisher Scientific	Cat# PBH5698
SelectScreen Kinase Profiling	SelectScreen Profiling, Thermo Fisher Scientific	Cat# A24800, A24801, A28578, A30526, A30527, A30528, A33688, A33689, A33690, PV3382, PV3412, PV3430, PV3432, PV3444, PV3459, PV3639, PV3707, PV3721
SelectScreen Nuclear Receptor Profiling	SelectScreen Profiling, Thermo Fisher Scientific	Cat# A15930, A15931, A15932
CyQUANT^{TM} LDH Cytotoxicity assay	Thermo Fisher Scientific	Cat# C20301
Deposited Data		
Crystal structure of rabbit skeletal muscle myosin MyHC IIb	This paper	PDB: 6YSY
Experimental Models: Cell Lines		
Human Adult Dermal Fibroblasts, adult (HDFa)	GIBCO, Thermo Fisher Scientific	Cat# C0135C
Human Lung Fibroblasts, (HLF)	Cell Applications Inc.	Cat# 506-05a
Sf9 cells in Sf-900 II SFM	GIBCO, Thermo Fisher Scientific	Cat# 11496-015
C2C12 mouse muscle myoblast	ATCC	Cat# CRL-1772
Experimental Models: Organisms/Strains		
Wistar albino rat, Han:WIST SPF	Toxi-Coop Ltd.	N/A
Recombinant DNA		
Plasmid: pFastBac1/NM2A/α-actinin/FLAG	This paper, Biomatik Co.	N/A
Plasmid: pFastBac1/NM2B/α-actinin/FLAG	This paper, Biomatik Co.	N/A
Plasmid: pFastBac1/NM2C/α-actinin/FLAG	This paper, Biomatik Co.	N/A
Plasmid: pFastBac1/NM2C-F490L/α-actinin/FLAG	This paper, Biomatik Co.	N/A
Plasmid: AdEasy/MYH7/GFP	Spudich Lab., Stanford University, (Kawana et al., 2017)	N/A
Software and Algorithms		
MATLAB 2019	MathWorks	https://www.mathworks.com/
Prism 8	GraphPad	https://www.graphpad.com:443/scientific-software/prism
Illustrator CS6	Adobe Systems	https://www.adobe.com/
Photoshop CS6	Adobe Systems	https://www.adobe.com/
MassLynx	Waters Ltd.	https://www.waters.com/

RESOURCE AVAILABILITY

Lead Contact

Further information and requests for resources and reagents should be directed to and will be fulfilled by the Lead Contact, András Málnási-Csizmadia (malna@elte.hu)

Materials Availability

MPH-inhibitors generated in this study will be made available on request, but we may require a payment and/or a completed Materials Transfer Agreement as there is potential for commercial application.

Data and Code Availability

The published article includes all datasets generated or analyzed during this study. The accession number for the skeletal myosin bound to MPH-220, Mg.ADP.VO_4 reported in this paper is PDB: 6YSY. The atomic model is available in the PDB (Berman et al., 2003).

EXPERIMENTAL MODEL AND SUBJECT DETAILS

Animals

200-250 g male Wistar rats were obtained from Toxi-Coop Ltd. (Hungary) or Animal Facility, Basic Medical Science Center at Semmelweis University (Hungary). Animals were maintained in standard housing conditions with 12-12-hour light-dark periods and were allowed free access to dry rat food and water. All procedures were conducted in accordance with the ARRIVE guidelines and the guidelines set by the European Communities Council Directive (86/609 EEC) and approved by the Animal Care and Use Committee of the Eötvös University (registration number: 48/1/2015) under the permission numbers: PE/EA/142-5/2020, PE/EA/143-7/2020.

Human muscle biopsies

Human muscle biopsy samples were prepared, processed and measured in accordance with the Recommended Standards for Muscle Biopsies by the European Reference Network for Neuromuscular Diseases and the European Commission and approved by the Regional Research Ethics Committee of the Coordination Centre of Clinical Studies of University of Pécs under the permission number: 8340–PTE 2020. *M.vastus* samples were obtained from female (60%) and male (40%) patients with normal creatine kinase (CK) levels and no or non-specific changes in muscle fibers. *M.soleus* sample was obtained from a female patient with normal creatine kinase (CK) level and non-specific changes in muscle fibers. 50% of patients had undergone electromyography (EMG) examination before biopsy preparation. Neither of the patients had received medications that would affect muscle protein compositions: obtained treatments include antihypertensive medicines, anti-inflammatory drugs and vitamin products.

METHOD DETAILS

Materials

All chemicals were purchased from Sigma-Aldrich (Germany) if otherwise not stated. Sulphobutyl-ether-β-cyclodextrin (Dexolve^{TM} (SBECD)) was obtained from Cyclolab (Hungary). HPLC-grade acetonitrile, chloroform and water were purchased from VWR (PA, USA). Blebbistatin was purchased from Sellekchem (TX, USA), AmBleb Várkuti et al., 2016 is product of Motorpharma Ltd., and isoflurane was purchased from Rotacher-Medical GmbH (Germany). Ames Microplate Format Mutagenicity Assay kit was purchased from Xenometrix (Switzerland).

Proteins

Rabbit actin was prepared as described previously from rabbit muscle acetone powder (Pel-Freez Biologicals Llc., AR, USA) (Spudich and Watt, 1971). Briefly, 5-6 g muscle acetone powder was soaked into ice cold G-actin Buffer (20 ml/g powder; 2 mM Tris pH 7.7, 0.2 mM CaCl2, 0.2 mM ATP, 2 mM DTT) and was stirred on ice for 40 min. After stirring wet acetone powder was filtered using filter paper. 2 mM MgCl2 and 50 mM KCl were added to the filtered solution and further incubated at room temperature for 30 min. KCl was added to the final concentration 0.5 M and was stirred for further 60 min. Solution was centrifuged (40,000 rpm, 90 min, 4°C) and pellet was homogenized in G-buffer and excessively dialyzed against G-buffer. After dialysis, solution was centrifuged (40,000 rpm, 90 min, 4°C) and the supernatant was frozen in liquid nitrogen in 1 mL aliquots. Skeletal muscle myosin subfragment-1 (S1) was prepared from rabbit *m.psoas* according to an earlier published protocol (Margossian and Lowey, 1982) by α-chymotryptic digestion (0.25 mg/ml α-chymotrypsin, 10 min, 25°C; reaction was stopped with 3 mM PMSF). Psoas S1 prep was further purified on MonoS 5/50 GL column to produce high-quality prep for crystallization. Cardiac muscle myosin S1 was isolated from left ventricle of porcine heart following cardiac myofibril preparation protocol (Tong et al., 2008) by α-chymotryptic digestion (0.05 mg/ml α-chymotrypsin, 10 min, 25°C; reaction was stopped with 3 mM PMSF). Human cardiac muscle myosin subfragment-1 (S1) was prepared from adult human left ventricular tissue samples obtained from ethically consented donors (AnaBios Corporation) according to earlier published protocol (Margossian and Lowey, 1982) by α-chymotryptic digestion (0.25 mg/ml α-chymotrypsin, 9 min, 25°C; reaction was stopped with 3 mM PMSF). Smooth muscle myosin S1 was prepared from chicken gizzard (Trybus, 2000) by activated papain digestion (Seidel, 1980) (0.2 mg/ml papain, 12 min, 25°C; reaction was stopped with 5 mM sodium iodoacetate). Human skeletal muscle myosin was prepared similarly to rabbit skeletal muscle myosin (Margossian and Lowey, 1982). Briefly, biopsies were washed in Rigor Buffer (20 mM MOPS pH 7.4, 40 mM KCl, 2 mM $MgCl_2$) and myosin was extracted in Myosin Extraction Buffer (20 mM MOPS pH 7.4, 500 mM KCl). Extracted myosin was precipitated in 21-volume ultrapure water with 1 mM EDTA. Myosin was collected in tabletop centrifuge, dissolved in Myosin Extraction Buffer and kept on ice until the measurement. The Sf9 codon optimized sequences for NM2 motor domains (Met^1-Arg^{775} for NM2A, Met^1-Arg^{782} for NM2B (B0) and Met^1-Arg^{799} for NM2C (C0)) fused to an Ala-Ser linker and an artificial α-actinin lever arm: (amino acid sequence: *AS*-EQTKS-DYLKRANELVQWINDKQASLESRDFGDSIE-SVQSFMNAHKEYKKTEKPPKGQEVSELEAIYNSLQTKLRLIKREPFVAPAGLTPNEIDST-WSALEKAEQEHAEALRIELKRQKKIAVLLQKYNRILKKLENWATTKSVYLGSNETGDSI-TAVQAKLKNLEAFDGECQSLEGQSNSDLLSI-LAQLTELNYNGVPELTERKDTFFAQQW-TGVKSSAETYKNTLLAELERLQKIED) as described earlier for NM2C (Heissler and Manstein, 2011)) with C-terminal FLAG-tag after an Ala-Leu linker (amino acid sequence: *AL*-DYKDDDK) sequences were synthesized and cloned into pFastBac1 expression vector. The NM2C-F490L construct was also synthesized by Biomatik Co in pFastBac1 expression vector. The pFastBac1/NM2 constructs were overexpressed in Sf9 cells after bacmid preparation from DH10Bac cells. To reduce proteolytic digestion during expression, Pepstatin-A (0.1 mg/l) was added to Sf9 cells (Gotoh et al., 2001). Expressed human β-cardiac myosin S1 (Kawana et al., 2017) was prepared as earlier described (Sommese et al., 2013).

ATPase measurement

Steady-state ATPase measurements were carried out in 50 μL volume in a flat bottom 384-well plate (Nunc-Thermo Fischer) using NADH-PK/LDH coupled assay described previously (Gyimesi et al., 2008). Briefly, myosin samples were mixed with 2% pyruvate kinase/lactate dehydrogenase (PK/LDH) mixture (Sigma P0294), 1 mM phosphoenol-pyruvate (PEP) and 200 μM NADH at 25°C in the presence of 0.5 mM ATP and 25 μM F-actin in ATPase buffer (10 mM MOPS pH 7.0, 4 mM $MgCl_2$, 2 mM β-mercaptoethanol) for 15 minutes. Absorbance was followed at 340 nm wavelength to follow the decrease of NADH in Microplate Spectrophotometer (BioTek Epoch). ATPase activity was calculated from linear regression of the time dependent absorbance data collected at 340 nm. Different concentrations of inhibitors were added to the reaction in 0.5 μL DMSO (1% of total volume). DMSO and actin-controls were measured for each measurement set.

Molecular dynamics simulation

Simulations were carried out using the AMBER16 program suite. The ff14SB force field (Maier et al., 2015) was used in all subsequent simulations to model protein interactions. The initial structure of the Fast Human Skeletal myosin-2 motor domain was modeled using structural homology with the SWISS-MODEL server (Waterhouse et al., 2018) using the Human Cardiac myosin-2 motor domain (PDB: 5N69). ADP.VO_4 was substituted to ADP.PO_4. Coordinates and partials charges for MPH-220 were refined using *antechamber* of the AMBERTOOLS package with the AM1 semi-empirical Hamiltonian. Force field parameters for the MPH-220 atoms were adopted from GAFF force field (Wang et al., 2004) based on structural similarity following the suggestions of the *parmchk2* program. We determined the initial position of MPH-220 by RMSD least-square fitting the model's structure with the blebbistatin-*Dyctiostelium* motor domain (PDB: 3BZ9) binding pocket. The initial position was then determined by RMSD least-square fitting the tricyclic ring of MPH-220 to blebbistatin's tricyclic ring. The water molecules resolved by crystallography were retained and the model was expanded in an 8-Angstrom clearance dodecahedron box with TIP3P water molecules for explicit solvation and counterions were added to neutralize the system's net charge. The complex was minimized with 2000 steps steepest descent followed by 4000 steps of conjugate gradient method while applying 10 kcal/(mol $Å^2$) to all atoms except water molecules. The minimization continued with the same protocol while removing the restraint from all H atoms. The same restraints were applied for the following steps. The complex was heated in 3 100-K 20-ps steps to 300 K under NVT conditions, then subsequently equilibrated to 1 bar in 20 ps under NPT conditions. NPT conditions were applied in all further steps. The system was cooled back to 10 K in the next 20 ps. Restraints from this point were only applied to the protein backbone. The system was heated back to 300 K in 10 ps and the simulation was continued for 1ns. The restraint force was then gradually reduced in 1 ns simulations steps to 5, 1, 0.5 and 0 kcal/(mol $Å^2$). The simulation was then allowed to continue and equilibrate under NPT conditions for a further 200 ns to obtain the final structures. The trajectories were sampled every 50 ps during the simulation.

Crystallization and data processing

MyCH IIb-MPH-220 crystals were obtained by vapor diffusion using a protein solution at 10 mg/ml containing 10 mM MOPS pH 7.3; 50 mM NaCl; 3 mM $MgCl_2$; 0.2 mM ATP; 3 mM NaN_3; 1 mM DTT; 0.1 mM EGTA; 0.1 mM PMSF; 1 μg/ml leupeptin, 2mM MgADP, 2mM VO_4, 0.5 mM MPH-220 against a reservoir containing 35% PEG600, 20mM DTT; 100mM HEPES pH 7.0; 5% DMSO at 291K. Optimization of crystallization conditions was performed with trypsin *in situ* proteolysis. Crystals were frozen then shot in the Proxima2 beamline (synchrotron Soleil). X-ray diffraction images were processed with AutoProc (Vonrhein et al., 2011). The crystal belongs to the $P2_12_12_1$ space group with one molecule per asymmetric unit. The data collection and refinement statistics are presented in Figure S3.

Structure determination and refinement

Structure of the motor domain was initially solved by molecular replacement using 1QVI (Gourinath et al., 2003) as a search model in Molrep (Vagin and Teplyakov, 2010), and completed with a second search for the lever arm and its essential light chain from 5N69 (Planelles-Herrero et al., 2017) with Phaser (McCoy et al., 2007). Refinement constraints for the ligand were automatically generated with Grade (Bricogne et al., 2017). The final model was obtained after several cycles of building in Coot (Emsley and Cowtan, 2004) and refinement with the latest 2019 release of BUSTER-TNT (Bricogne et al., 2017).

Isometric force measurement

Isometric force of rat left hindleg was measured by a force meter (Supertech Ltd.) after the hindleg was fixed and stimulated according to earlier published protocol (Pratt and Lovering, 2014). A non-elastic wire was attached to the ankle of the rat and pulled until pre-strained position. Spike$^{(R)}$ software controlled stimulator (BioStim, Supertech Ltd.) was used to trigger the *n. femoralis* through metal electrodes with 100 Hz, 1 s, 4V, 2.5 minute intervals. Data detection was performed with CED Micro 1401 data acquisition interface. Inhibitors were either dissolved in 200 μL DMSO for intraperitoneal injection or in 1ml 30% SBECD solution (dissolved in GIBCO^{TM} Dulbeccos's Phosphate Buffered Saline (D-PBS)) for oral administration.

Non-invasive measurement of cardiovascular and respiratory functions

Cardiovascular and respiratory functions were measured using a non-invasive pulse oximeter (MouseOx Plus, Starr Life Sciences Corp., PA, USA). Blood flow parameters shown on figures corresponds to the measured pulse distention, which is the measure of change in blood vessel volumes in the light path of the sensor, which reflects local blood pressure changes. Rats were anesthetized and the neck region was trimmed using a small animal trimmer to facilitate accurate measurements by size specific collar sensor.

Concentration measurement from tissue samples

Animals were treated *i.p.* or *per os* with MPH-220, over-anesthetized and tissue samples were collected and frozen at −80°C. Tissue samples were thawed and homogenized in D-PBS, and chloroform was added to the homogenate. Samples were thoroughly shaken, vortexed and sonicated. After sonication, samples were centrifuged and the chloroform layer was collected. Chloroform extraction was repeated two more times. Chloroform was evaporated in a fume-hood. After chloroform drying, water-acetonitrile solution (50%/50%) was added to the samples, which were again vortexed and sonicated again. Samples were centrifuged and supernatants were collected and transferred into ultra-centrifuge vials and ultracentrifuged at 60,000 rpm, 10°C for 60 minutes before HPLC-MS injection. Peak area of compound in HPLC was determined at 400 nm and concentration of compound was determined from the calibration curve. HPLC-MS conditions were the following: Merck Purosphere STAR RP-18 endcapped 250 mm X 4.6 mm column, mobile phase: isocratic 50% H_2O (0.1% TFA) – 50% ACN (0.09% TFA), injection volume: 20 μL HPLC, flow rate: 0.5 ml/min, run time: 25 min, detection at 260, 280, 300, 400 and 450 nm, capillary voltage: 3.5 kV, cone voltage: 30 V.

Spasticity animal model

Targeted brain damage was performed to establish a rat model of spastic cerebral palsy. Briefly, animals were pre-anesthetized with 4% isoflurane, which was reduced to 2% after the fixation of the animal on the stereotactic apparatus. First, a 2 cm-long longitudinal incision between ears was carried out, which was followed by the cleaning of the surface of the skull by hydrogen peroxide to visualize the Bregma point. Injection coordinates were determined based on The Rat Brain in Stereotaxic Coordinates, 6th Edition (Paxinos and Watson, 2007): ML −0.8 mm, AP −10 mm and DV 9.7 mm from the dura. A 25 μl Neuros Syringe (Hamilton, NV, USA) with needle size 22G was used to gently inject 15 μl ethanol for left pyramidal tract lesion. After the injection the syringe was left in place for 10 minutes, followed by its removal from the brain and the sealing of the wound.

Neural network based deep-learning analysis of movements in open-field tests

The over-ground locomotion of the animals was recorded in an 80 by 80 cm wide plastic open-field box using an 8 mm thick transparent Plexiglas as the bottom panel over the course of 15 minutes. The arena was placed on a custom-made wooden frame in order to raise it 1 m above the ground level, while keeping the transparent bottom unobstructed. A Microsoft Kinect V2 for XBOX ONE (2013) RGB-D sensor was secured approx. 80 cm below the Plexiglas facing upward to capture depth information from inside the open-field arena (Figure 4B). The Kinect sensor was connected to a Windows PC (i5-9500F, GeForce GTX 1050 2 GB, 16GB DDR4) placed in a separate room via the official adaptor (Kinect Adaptor for Windows PC) and a USB extension cable. The Kinect for Windows SDK V2.0.1410.19000 API-s were used to control the Kinect sensor in MATLAB v. R2019b with the Image Acquisition Toolbox Support Package for Kinect for Windows Sensor add-on.

An in-house MATLAB program was used to calibrate the spatial position of the device by measuring the relative distance of the four corners of the arena to the sensor to ensure uniform depth information values in the whole arena during experiments. Another in-house MATLAB program was used for image acquisition by the infrared depth camera (512 × 424 / 30 FPS) and the RGB camera (1920 × 1080 / 30 FPS) simultaneously. Video recordings from the depth camera were stored in .mj2 archives using lossless 16-Bit Motion JPEG 2000 compression, while the RGB camera recordings were stored in MP4 formats to allow easy viewer access. The depth video recordings were subjected to a preprocessing MATLAB script to correct the erroneous depth estimates arising from the time-of-flight depth sensing, such as flying pixels and multipath interference. The modified archives were scaled to preserve intensity values of the region of interest (rat in the arena) and exported as 8-Bit uncompressed AVI videos for further use.

A Resnet-50 deep convolutional neural network was trained to predict distinct body parts (nose, neck, center, right forelimb, left forelimb, right hindlimb, left hindlimb, base of the tail) of the animals on the 8-Bit depth recordings using the DeepLabCut toolbox (Mathis et al., 2018) in the Google Colaboratory python environment. The network training parameters were identical as described in Nath et al. (2019) with the provided pre-trained resnet_v1_50 architecture using stochastic gradient descent optimizer, multi-step learning rate (0,005 until 10000 epochs, 0.02 until 430.000, 0.002 until 500.000), batch size of 1, train-test split of 0.3, and no early stopping. We used ~1000 manually annotated frames for the final training and validation sets (training on 500.000 epochs achieved 1.75 mean pixel error for the training and 7.33 mean pixel error for the validation set). A custom MATLAB script was then used to process the previously modified depth archives (25.000 frames / recording) in conjunction with the error corrected numerical output (X and Y coordinates) of the deep learning algorithm of each labeled body part. The animals were first segmented based on the pixel intensity deviation relative to the background. Each frame was then translated and rotated based on the position and angle of the axis between the center of mass of the animal and the position of its nose to create egocentric recording. This transformation and rotation was then carried out on the body part labels as well. The 3 dimensional position of each limb was calculated by combining the transformed output coordinates of the deep neural net with the depth information of the labeled body parts on each frame of the preprocessed and transformed depth recordings. The three dimensional movement maps were exported to further analyses.

In the final algorithm 95% CI least-squares elliptical fittings were computed on the 3D movement maps of each individual limb of the animals and the gait parameters were calculated (Table S3). Centroid displacement thresholds on moving average function of 100 frames were used to calculate distinct locomotion regimes (1^{st} Regime: < 0.6 pixel deviation, 2^{nd} Regime: > 0.6 and < 1.2 pixel deviation, 3^{rd} Regime: > 1.2 pixel deviation.). The gait parameters were scaled using the Z-score method and subjected to principal component analysis and the results were represented in the 3D PC space together with the 95% CI ellipsoids.

Cylinder assay

Motor functions of spastic rats were tested in an open-top, 21 cm diameter, clear plastic cylinder. Forelimb activity was calculated from number of touches of each forelimb against the wall of the arena. Forelimb touch was defined when the whole palm touched the sidewall of the cylinder. Number of sidewall touches was counted for 3 minutes.

Safety panel measurements

G-protein coupled receptor inhibition and activation was tested in the gpcrMAX panel of DiscoverX® Profiling service (Eurofins). Caco-2 assays were carried out by Absorption and Permeability Services at Eurofins Discovery. Predictor^{TM} hERG Fluroescence Polarization Assay, SelectScreen Kinase Profiling and SelectScreen Nuclear Receptor Profiling was carried out by Thermo Fisher Scientific. Ames MPF^{TM} (Xenometrix, Switzerland) reverse mutagenicity assay was performed according to the manufacturer's guide on TA98 and TA100 bacterial strains in the absence and presence of phenobarbital/β-naphtoflavone-induced rat liver S9 fraction. Cytotoxicity measurements were performed with CyQUANT^{TM} LDH Cytotoxicity assay (Thermo Fisher) according to the manufacturer's protocols with human adult dermal (GIBCO, Thermo Fisher) and lung (Cell Applications Inc., CA, USA) fibroblast strains.

QUANTIFICATION AND STATISTICAL ANALYSIS

Unless otherwise specified, data are presented as means with standard deviations. Principal component analysis data are presented as box and whishkers representation with min to max whiskers in GraphPad Prism software (Graphpad Software Inc.). ATPase activity analysis, IC_{50} and maximal inhibition analysis, single exponential fitting and t tests for significance analysis were performed by GraphPad Prism software (Graphpad Software Inc.). Tissue concentration determination was based on standard curve fitting and area under curve analysis by MassLynx software (Waters Ltd.). Principal component analysis was performed by MATLAB software (MathWorks). We did not apply statistical methods to predetermine sample sizes for animal experiments and kept the used subject numbers at a minimum to conform with ARRIVE and 3R principles. Further details of statistical analysis can be found in the figure legends or in the Method Details section.

Supplemental Figures

A

gene	MYH1	MYH2	MYH3	MYH4	MYH6	MYH7	MYH8	MYH9	MYH10	MYH11	MYH13	MYH14
myosin-2 isoform	MyHC IIx/d	MyHC IIa	embryonic skeletal	MyHC IIb	α-cardiac	β-cardiac/ MyHC I	perinatal skeletal	NM2A	NM2B	smooth	extraocular	NM2C
human	L	L	L	L	F	F	L	F	F	F	L	F
rat			L	L	F	F		F	F	F		
pig	L	L		L		F						
dog	L	L		L		F	L	F			L	
chicken	L		L					F		F		
rabbit				L						F		
cow	L	L				F			F			
mouse	L		L	L	F	F	L	F	F	F		F

gene	MYSA/MYO2	MYSN
myosin-2 isoform	muscle	non-muscle
Drosophila	F	F
C.elegans	F	

MYH1 (MyHC IIx/d - fast)

```
human        LDIAGFEIFDFNSLEQLCINFTNEKL
pig          LDIAGFEIFDFNSLEQLCINFTNEKL
dog          LDIAGFEIFDFNSLEQLCINFTNEKL
chicken      LDIAGFEIFDFNSLEQLCINFTNEKL
cow          LDIAGFEIFDFNSLEQLCINFTNEKL
mouse        LDIAGFEIFDFNSLEQLCINFTNEKL
             **************************
```

MYH2 (MyHC IIa - fast)

```
human        LDIAGFEIFDFNSLEQLCINFTNEKL
pig          LDIAGFEIFDFNSLEQLCINFTNEKL
dog          LDIAGFEIFDFNSLEQLCINFTNEKL
cow          LDIAGFEIFDFNSLEQLCINFTNEKL
             **************************
```

MYH3 (embryonic skeletal - fast)

```
human        LDIAGFEIFEYNSLEQLCINFTNEKL
rat          LDIAGFEIFEYNSLEQLCINFTNEKL
mouse        LDIAGFEIFEYNSLEQLCINFTNEKL
chicken      LDIAGFEIFDFNSLEQLCINFTNEKL
             *********::***************
```

MYH4 (MyHC IIb - fast)

```
human        LDIAGFEIFDFNSLEQLCINFTNEKL
pig          LDIAGFEIFDFNSLEQLCINFTNEKL
dog          LDIAGFEIFDFNSLEQLCINFTNEKL
rabbit       LDIAGFEIFDFNSLEQLCINFTNEKL
rat          LDIAGFEIFDFNTLEQLCINFTNEKL
mouse        LDIAGFEIFDFNTLEQLCINFTNEKL
             ************:*************
```

MYH6 (α-cardiac)

```
human        LDIAGFEIFDFNSFEQLCINFTNEKL
rat          LDIAGFEIFDFNSFEQLCINFTNEKL
mouse        LDIAGFEIFDFNSFEQLCINFTNEKL
             **************************
```

MYH7 (β-cardiac, MyHC I – slow)

```
human        LDIAGFEIFDFNSFEQLCINFTNEKL
rat          LDIAGFEIFDFNSFEQLCINFTNEKL
pig          LDIAGFEIFDFNSFEQLCINFTNEKL
dog          LDIAGFEIFDFNSFEQLCINFTNEKL
cow          LDIAGFEIFDFNSFEQLCINFTNEKL
mouse        LDIAGFEIFDFNSFEQLCINFTNEKL
             **************************
```

MYH8 (perinatal skeletal)

```
human        LDIAGFEIFDFNSLEQLCINFTNEKL
dog          LDIAGFEIFDFNSLEQLCINFTNEKL
mouse        LDIAGFEIFDFNSLEQLCINFTNEKL
             **************************
```

MYH9 (NM2A)

```
human        LDIAGFEIFDLNSFEQLCINYTNEKL
rat          LDIAGFEIFDLNSFEQLCINYTNEKL
dog          LDIAGFEIFDLNSFEQLCINYTNEKL
mouse        LDIAGFEIFDLNSFEQLCINYTNEKL
chicken      LDIAGFEIFELNSFEQLCINYTNEKL
             *********:****************
```

MYH10 (NM2B)

```
human        LDIAGFEIFELNSFEQLCINYTNEKL
rat          LDIAGFEIFELNSFEQLCINYTNEKL
cow          LDIAGFEIFELNSFEQLCINYTNEKL
mouse        LDIAGFEIFELNSFEQLCINYTNEKL
             **************************
```

MYH11 (smooth)

```
human        LDIAGFEIFEVNSFEQLCINYTNEKL
rat          LDIAGFEIFEVNSFEQLCINYTNEKL
rabbit       LDIAGFEIFEVNSFEQLCINYTNEKL
mouse        LDIAGFEIFEVNSFEQLCINYTNEKL
chicken      LDIAGFEIFEINSFEQLCINYTNEKL
             **********:***************
```

MYH13 (extraocular skeletal)

```
human        LDIAGFEIFDFNSLEQLCINFTNEKL
dog          LDIAGFEIFDFNSLEQLCINFTNEKL
             **************************
```

MYH14 (NM2C)

```
human        LDIAGFEIFQLNSFEQLCINYTNEKL
mouse        LDIAGFEIFQLNSFEQLCINYTNEKL
             **************************
```

MYSA/MYO2 (muscle)

```
Drosophila   LDIAGFEIFEYNGFEQLCINFTNEKL
C.elegans    LDIAGFEIFDFNSFEQLWINFVNEKL
             *********::*.**** ***.****
```

MYSN (non-muscle)

```
Drosophila   LDMAGFEIFELNSFEQLCINYTNEKL
```

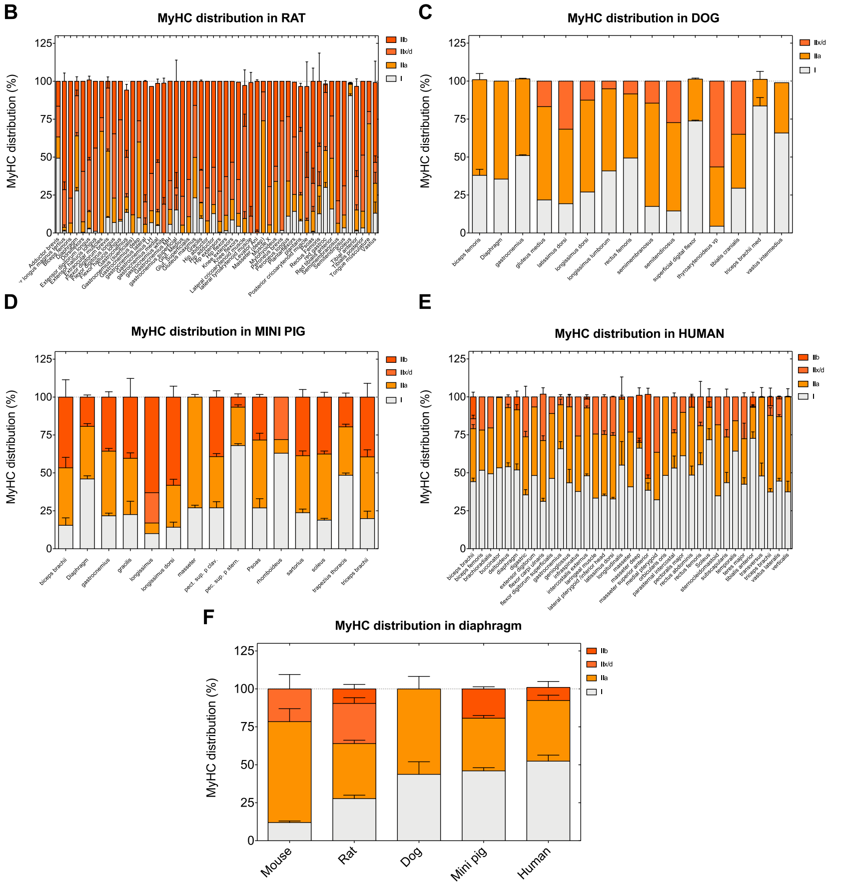

(legend on next page)

Figure S1. Sequence Analysis of Myosin-2 Isoforms from Different Species, Related to Figure 1

(A) The tables show the amino acid residue at the starting point of the HP-helix in myosin-2 isoforms expressed from different MYH genes in eight vertebrate species and the muscle and non-muscle myosin-2 isoforms in *D. melanogaster* and *C. elegans* invertebrate species. The alignments below the tables represent the sequence environment of the relevant Leu (blue L) or Phe (black F) residue, including the switch-2 loop (red) and the N-terminal part of the HP-helix (light orange). These data clearly show that all fast skeletal myosin-2 isoforms in all species contain Leu in the morpholine-interacting position, while Phe is present in all slow type myosin-2 s including both cardiac isoforms at this position. The characteristic difference is even more pronounced when comparing the neighboring residues in the HP-helix, which are practically invariant in all myosin isoforms and species. (B-F) Myosin-2 isoform distribution within different muscle types in different species. Literature-based analysis of myosin-2 isoform composition – determined by SDS-PAGE or immune/enzyme histochemistry – of different muscles in rat (B), dog (C), mini pig (D) and human (E) show significant differences in the proportion of the slow isoform (MyHC I, gray) between the species. While rat muscles contain predominantly fast isoforms (MyHC IIa, IIb, IIx/d, orange), the ratio of fast isoforms in human muscles is between 40%–70%. Distributions in dogs and mini-pigs are in between the rat and human levels. These differences bear important consequences on the expected effect size in different species and may require unique consideration of dosage in non-clinical studies on different species (e.g., rats versus dogs/pigs). The relatively high proportion of slow isoform in human muscles also has important positive consequence on the effect profile of an MPH-220 based anti-spastic drug, because overdosing-related complete muscle tone loss is not expected to occur due to the residual non-inhibited slow myosin contractions. This latter condition confers a huge advantage over the currently used nervous system targeting muscle relaxants, where temporary but complete immobility can occur in case of slight overdose. The large difference in slow isoform proportion can also be seen in the diaphragm of different species (F), which indicates that MPH-220 will be even safer for respiratory functions in humans than in rats.

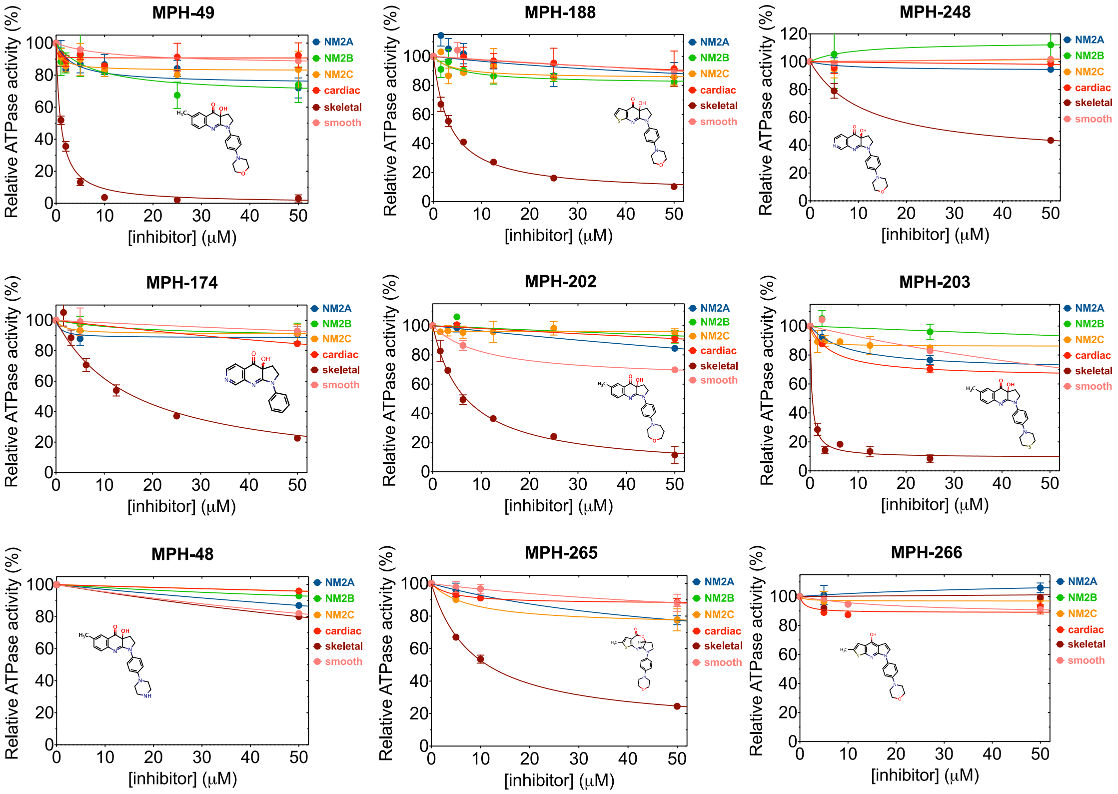

Figure S2. Inhibitory Properties of Different MPH-220 Derivatives, Related to Figure 1

Relative ATPase activities are shown for different MPH-220 derivatives tested during the development of MPH-220. MPH-49 is the morpholine derivative of blebbistatin, which shows selective inhibition; however, its solubility remained blebbistatin-like (less than 50 μM in aqueous solutions). MPH-188 and MPH-248 are morpholine derivatives on different scaffolds of the patented MPH-family. MPH-188 showed drastic improvement in solubility (1 mM in aqeous solutions), but its IC_{50} value for skeletal myosin was slightly worse than that of MPH-220. MPH-248 retained skeletal myosin specificity of the pyridine ring containing core (MPH-174), but its total inhibition and IC_{50} values remained worse than those of MPH-220. We found that the morpholino group (MPH-49) was superior to homo-morpholine (MPH-202), thiomorpholine (MPH-203) or piperazine (MPH-48). The IC_{50} of MPH-203 was promising; however, its solubility was even lower than that of MPH-49, suggesting that the optimal ring structure for selective and efficient inhibition is the morpholine ring. We also tried to modify the ring structure of the tricyclic core, but neither modification showed improved properties, confirming that MPH-220 is the optimal structure. Mean ± SD are shown in all ATPase experiments; n = 3–9.

A

Pre-power-stroke (ADP.VO_4) state	MyHC IIb + MPH-220
Data collection	
Space group	P 2_1 2_1 2_1
Cell dimensions	
a, *b*, *c* (Å)	49.6 119.4 176.6
a, b, g (°)	90.0 90.0 90.0
Resolution (Å)	88.3 - 3.3 (3.4 - 3.3)*
R_{merge}	0.003722 (0.2293)
I / s*I*	10.46 (2.42)
$CC_{1/2}$	0.999 (0.939)
Completeness (%)	99.80 (99.88)
Redundancy	2.0 (2.0)
Refinement	
Resolution (Å)	3.3
No. reflections	total: 34625 (3374) unique: 17313 (1687)
R_{work}	0.2260 (0.3450)
R_{free}	0.2464 (0.4555)
Non-hydrogen atoms	7474
Protein	7382
Ligand/ion	60
Water	32
B-factors	100.49
Protein	100.73
Ligand/ion	91.05
Water	62.66
R.m.s. deviations	
Bond lengths (Å)	0.015
Bond angles (°)	1.55

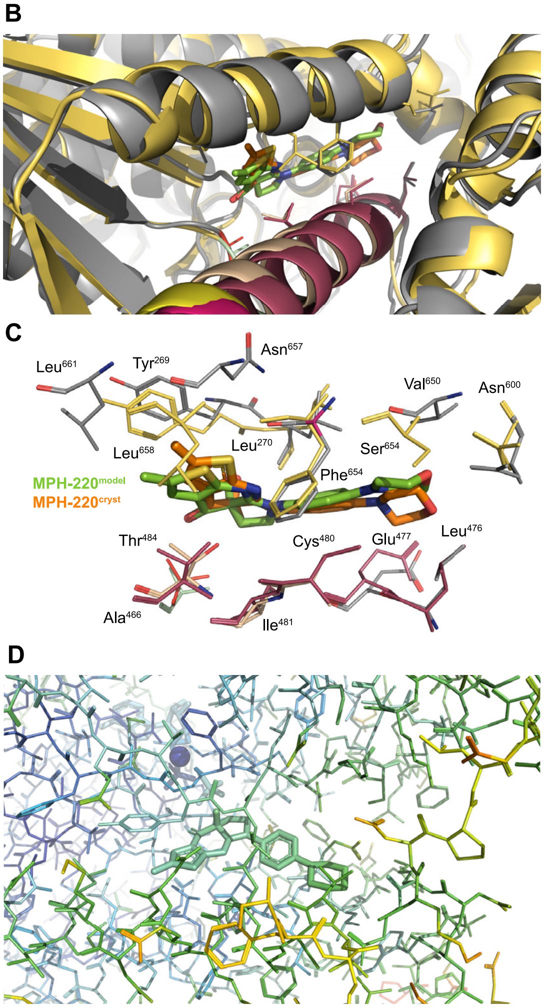

Figure S3. Crystal Structure Refinement Statistics and Comparison of Crystal and Modeled Structures Used for Inhibitor Development, Related to Figure 2

(A) Data collection and refinement statistics (molecular replacement). Data from one crystal. *Values in parentheses are for highest-resolution shell. (B) Cartoon representation of the crystal structure of MyHC IIb (gray/beige), and the superimposed modeled structure of MyHC IIa from molecular dynamic simulations (yellow/maroon). MPH-220 binding site reveals that the position and orientation of MPH-220 in the crystal structure (orange) and in the modeled structure (green) is similar. Amino acid residue carbons in gray (crystal structure) and maroon (model), and carbons for MPH-220 in orange (crystal structure) and green (model) are shown. (C) Close-up of the MPH-220 binding site reveals that HP-helix position is well predicted; in particular, Leu^{476} position is very similar. The alignment also reveals a moderate shift in MPH-220 position between the homology model and the crystal structure; in particular we see slightly different position and orientation of the morpholino group. Still, the homology model predicts well the sub-pocket explored by this cycle; residues Leu^{476}, Glu^{477}, Cys^{480}, Asn^{600} and Val^{650} interact indeed with the morpholino group in both crystal structure and homology model. These results confirm that the modeled structure that we used for inhibitor development (*cf.* Figures 1 and S2) is reliable and the results from those experiments are trustworthy. (D) Close-up view of the crystal structure with bound MPH-220 colored according to B-factors from 21.1 Å^2 (dark blue) to 125.2 Å^2 (red). ADP, VO_4 and MPH-220 are represented by thicker lines, the sphere represents the Mg^{2+} ion.

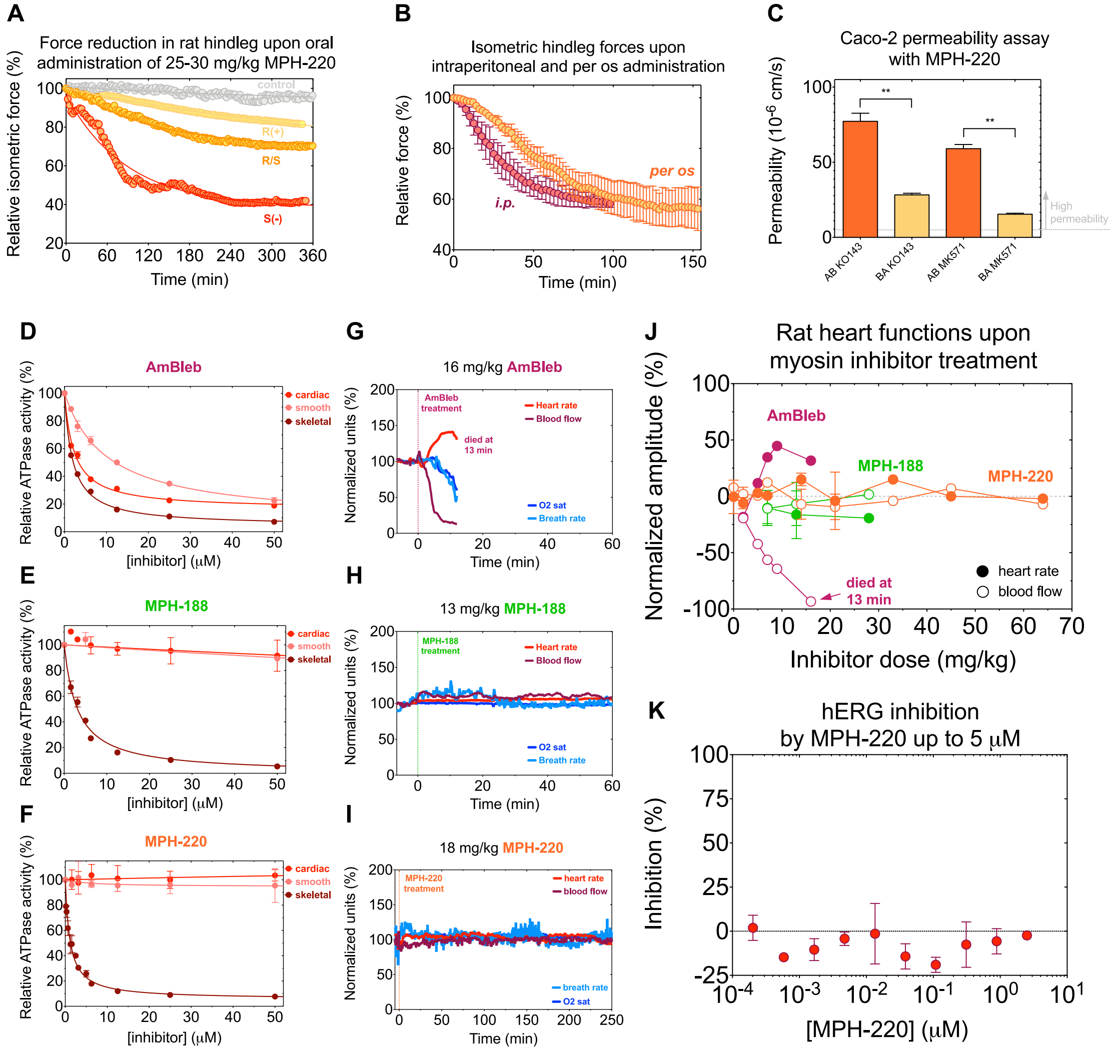

Figure S4. MPH-220 Effects on Isometric Force and Vital Functions, Related to Figure 3

(A) Isometric force reduction in rat hindleg after oral MPH-220 treatment: $\Delta F_{S(-)} = 58\%$, $\Delta F_{R(+)} = 36\%$, $\Delta F_{R/S} = 32\%$, $\tau_{S(-)} = 88$ min, $\tau_{R(+)} = 121$ min, $\tau_{R/S} = 461$ min; muscle fatigue in the control animals: $\Delta F_{contr} = 8\%$, $\tau_{contr} = 323$ min. (B) 18 mg/kg MPH-220 was administered to anesthetized rats by intraperitoneal injection in 200 μL DMSO (pink circles) or orally through a gavage tube in 30% SBECD (orange circles). Isometric force decrease rates were very similar ($\tau_{i.p.} = 34$ min) except that oral administration resulted in a 17-minute leg phase – corresponding to absorption of MPH-220 – followed by force decrease phase ($\tau_{p.o.} = 53$ min). Mean ± SD are shown; n = 2. These observations support high gastrointestinal permeability of MPH-220, which was further confirmed by *in vitro* Caco-2 permeability assay (C). (C) Caco-2 permeability assay in the apical-to-basolateral (AB, orange) and basolateral-to-apical (BA, light orange) direction in the presence of two different transporter inhibitors. Mean ± SD are shown; n = 2 (D-F) ATPase activity of skeletal (brown), cardiac (red) and smooth (pink) muscle myosins, measured in the presence of non-selective para-aminoblebbistatin (AmBleb) (D), MPH-188 (E) and MPH-220 (F). Mean ± SD are shown; n = 3-12. (G-I) All three inhibitors were administered to rats in different concentration ranges and cardiovascular (heart rate, blood flow) and respiratory functions (breath rate, oxygen saturation) were monitored. 16 mg/kg AmBleb killed the animals within 15 minutes due to heart failure (G), while neither 13 mg/kg MPH-188 (H) nor 18 mg/kg MPH-220 (I) had any significant effect on cardiovascular and respiratory functions. Note that we measured MPH-220 effect on longer timescales (parallel with force measurements). (J) We repeated the experiments several times and found that MPH-220 does not affect cardiac functions to a greater extent than the solvent excipient during the long anesthetic period (*cf.* Figures 2E and 2F). Data are mean ± SD, n = 1-4. (K) hERG potassium channel inhibition measurement up to 5 μM MPH-220. We measured hERG inhibition up to 5 μM, because the concentrations of MPH-220 in cardiac tissue even upon treatment with high doses (up to 130 mg/kg) were in this concentration range (3-7 μM). At this concentration range we did not observe inhibition of hERG potassium channels and we did not observe any concentration dependence of inhibition on cardiomyocytes, which would otherwise potentiate a drug candidate for QT prolongation leading to life-threatening arrhythmias (Pollard et al., 2010). Mean ± SEM are shown; n = 2.

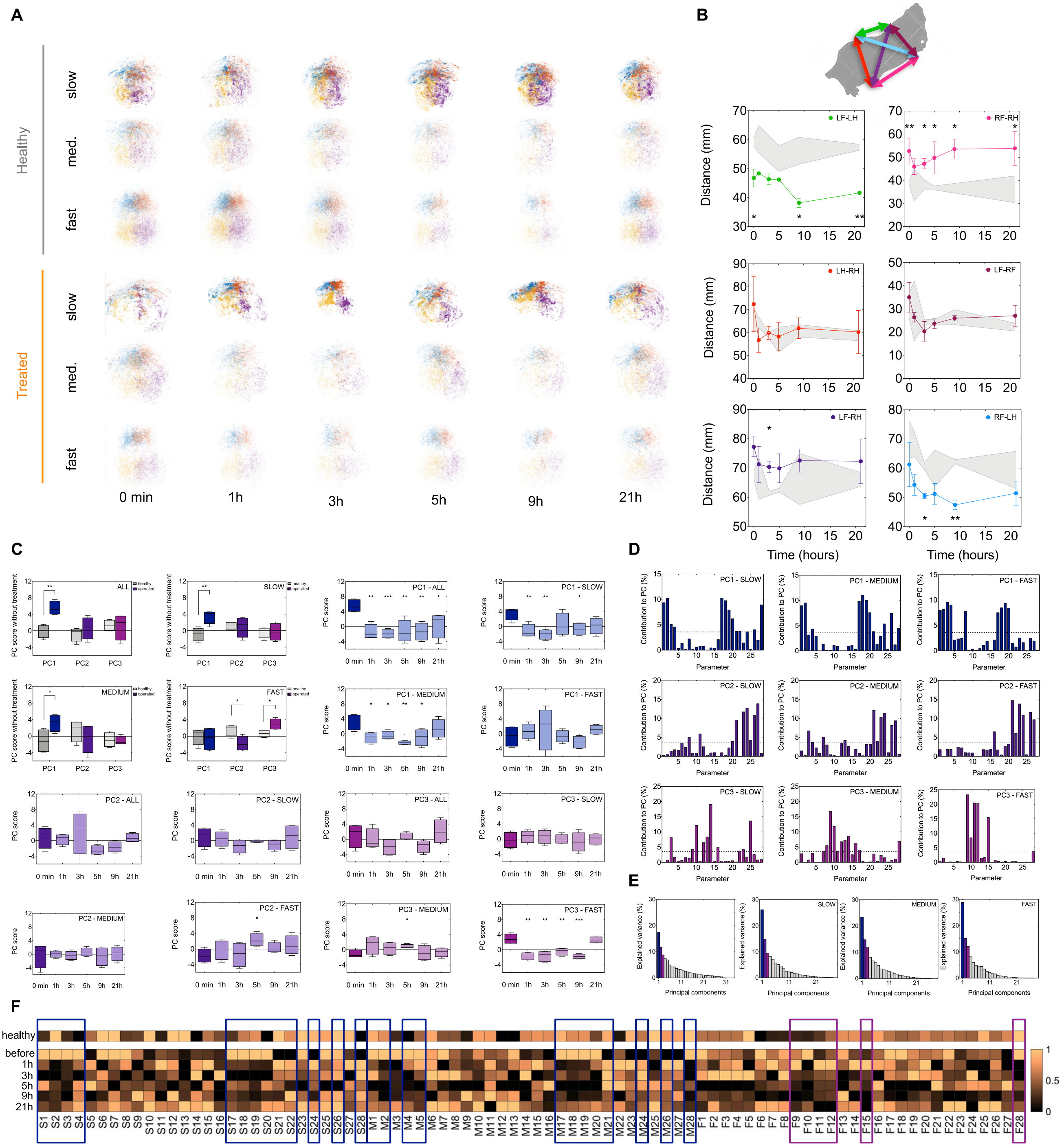

MPH-220 effect
in slow and medium
regimes (PC1)

MPH-220 effect
in fast regime
(PC3)

MPH-220 effect
in slow and medium
regimes (PC1)

Length of X-Y major axis					Length of X-Z major axis			Angle of X-Y major axes				Angle of X-Z major axes				Volume						Distance				Body-axis	No. of frames
LF	RF	LH	RH	LF	RF	LH	RH	LF	RF	LH	RH	LF	RF	LH	RH	LF	RF	LH	RH	LF-RF	LF-LH	LF-RH	RF-LH	LH-RH	RF-RH		
1	2	3	4	5	6	7	8	9	10	11	12	13	14	15	16	17	18	19	20	21	22	23	24	25	26	27	28

(legend on next page)

Figure S5. Gait Analysis of MPH-220-Treated Rats, Related to Figures 4 and 5

(A) Paw position distribution of healthy (upper three rows) and treated (lower three rows) animals in the three speed-regimes (slow (less than 0.036 m/s), medium (0.036-0.072 m/s) and high (more than 0.072 m/s)), 1, 3, 5, 9 and 21 hours after the first measurement (healthy control) or before and 1, 3, 5, 9 and 21 hours after 20 mg/kg oral MPH-220 treatment. (B) Averaged distances between the paws in each frame of the 3D recordings in healthy (gray band) and treated (colored dots) animals; green: left fore- and hindlimbs, pink: right fore- and hindlimbs, red: left and right hindlimbs, maroon: left and right forelimbs, purple: left fore- and right hindlimbs, blue: right fore- and left hindlimbs. Schematic representation of distances is shown above the plots. Statistical analyses show that left fore- and hindlimbs are significantly closer in the operated rats than in the healthy animals, however, 1-5 hours after MPH-220 treatment the difference becomes insignificant. The right fore- and hindlimbs are significantly farther in the operated rats before treatment, which becomes non-significant 1 hour after MPH-220 treatment. These together indicate that MPH-220 treatment resulted in a significantly straightened body axis. Data are mean ± SD; n = 2. (C) Principal component (PC) analysis: PC1, PC2 and PC3 scores of healthy (gray) and operated (colored bars) rats in all, slow, medium-speed and fast movement regimes (upper left quartet). PC1 (blue, upper right quartet), PC2 (eggplant, lower left quartet) and PC3 (purple, lower right quartet) scores before (darker) and after (lighter) 20 mg/kg oral MPH-220 treatment in all, slow, medium-speed and fast movement regimes. Boxplots with min-to-max whishkers, n = 4. (D) Parameter contributions to PC1 (upper row), PC2 (middle row) and PC3 (lower row) in the slow (left column), medium-speed (middle column) and fast (right column) movement regimes. Dotted lines represent the threshold for major contributions to PC (3.57%). Boxplots with min-to-max whishkers, n = 4. (E) Explained variance in all, slow, medium-speed and fast movement regimes; PC1, PC2 and PC3 are colored according to panels C-D. (F) The computed gait parameters were scaled (Z-score) and averaged. The columns represent the individual gait parameters (1-28, defined below the heatmap) in the slow (S1-28), medium-speed (M1-28) and fast (F1-28) movement regimes. The separate row represents the average of healthy animals at zero minute, and the other six rows represent the parameter scores before and 1, 3, 5, 9 and 21 hours after MPH-220 treatment (n = 4). PC analysis revealed that in the slow regime MPH-220 has the largest effect on X-y axis length and the consequent volumes of the ellipsoids representing paw positions in 3D and certain distances between the centers of ellipsoids (blue brackets) contributing to PC1; in the fast regime MPH-220 has the largest effect on the angles of the ellipsoids (purple brackets) contributing to PC3. Parameter description used in PCA calculations: video recordings were analyzed in three walking speed categories. The numbers encode different parameters of the ellipsoids fitted to data points from 3D position analysis. LF: left front limb, RF: right front limb, LH: left hind limb, RH: right hind limb.

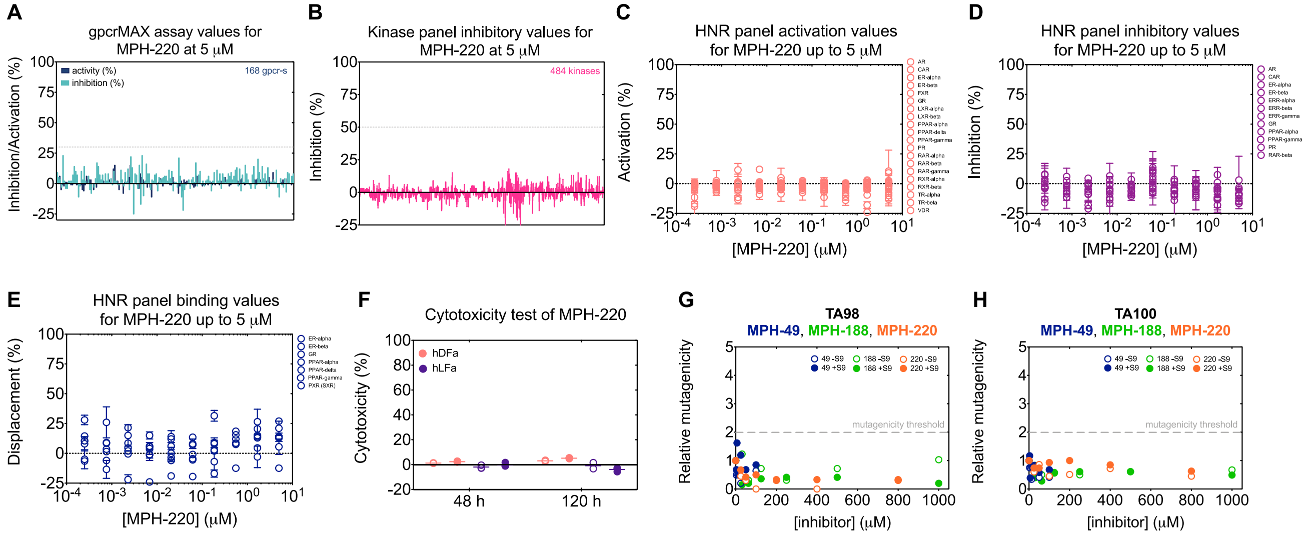

Figure S6. Safety Profiling of MPH-220 Supports Further Drug Development due to Lack of Mutagenicity and Interaction with Off-Target Enzymes, Related to STAR Methods

(A) We tested the effects of 5 μM MPH-220 on 186 different human G-protein-coupled-receptors (GPCRs) covering 60 different receptor families including adrenergic, dopamine, P2Y and serotonin receptor families (by DiscoverX-Eurofins). According to the highly selective nature of MPH-220, neither GPCR was inhibited or activated above 30%, which is a standard reference threshold for hit compounds. (B) Beside the gpcrMAX panel, inhibition of 484 kinases was measured in the presence of 5 μM MPH-220. Neither kinase was inhibited by more than 20%, which indicates that MPH-220 does not interfere with the signal transduction pathways in human cells. This Select Screen Kinase Profiling panel (by Thermo Fisher) contains all available wild-type and the most abundant mutant forms of human kinases. (C-E) MPH-220 was also tested on 23 human hormone nuclear receptors (HNR) at 5 μM concentration (by Thermo Fisher). In agreement with the kinase and GPCR results, all investigated receptors remained unaffected by MPH-220 due to the lack of significant binding to any of the HNRs. Mean ± SEM are shown; n = 2 in (A-E). (F) Cytotoxicity was measured with CyQUANT^{TM} LDH Cytotoxicity assay on human adult dermal fibroblast (hDFa, pink) and human adult lung (hLFa, purple) fibroblast cell lines in the presence of 20 μM (open circles) and 50 μM (closed circles) MPH-220 for 48 and 120 hours. MPH-220 was not toxic to either fibroblast strain at any time point or concentration, confirming its safe use in further developments. As one of the most important requirements for a lead compound, mutagenicity was measured by the OECD/FDA approved Ames reverse mutagenicity assay using the two most sensitive bacterial strains for testing frameshift (TA98, G) and base-pair substitution (TA100 H) mutation both in the absence (open circles) and presence (closed circles) of activated rat liver S9 fraction. Relative mutagenicity did not show MPH-220 concentration dependency and, more importantly, experiments on neither strain resulted in any data points above the threshold (gray dotted line). Besides MPH-220 we also tested the mutagenicity of the other two morpholine derivatives of MPH-220 (*cf.* Figure S2) to elucidate whether the lack of mutagenicity is associated with the morpholine group. Neither MPH-49 nor MPH-188 showed concentration dependent increase in mutagenicity levels and, more importantly, neither showed in data points above the OECD/FDA threshold. Lack of mutagenicity was observed for both TA98 and TA100 *S.typhimurium* strains both in the absence and presence of liver S9 fraction, suggesting that neither the inhibitors nor their major metabolites are mutagenic, which supports safe development of MPH-220 toward human clinical phases.